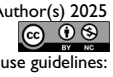
Check for updates

Research Paper

EARTHQUAKE SPECTRA

Earthquake Spectra
2025, Vol. 41(5) 3826–3857
© The Author(s) 2025

Article reuse guidelines:
sagepub.com/journals-permissions
DOI: 10.1177/87552930251377781
journals.sagepub.com/home/eqs


Assessment of seismic design provisions for floor diaphragms and higher-mode responses using data from instrumented buildings in California

C. Franco Mayorga, M.EERI, and Georgios Tsampras, M.EERI

Abstract

This article assesses the seismic design provisions for floor diaphragms per ASCE/SEI 7-22 Section 12.10.1 and Section 12.10.3, with emphasis on how these provisions account for the higher-mode effects on peak horizontal floor accelerations of earthquake-resistant buildings. A framework is developed for processing and analyzing strong-motion acceleration data from buildings monitored by the California Strong Motion Instrumentation Program (CSMIP), which is used to assess the floor diaphragm design acceleration coefficients in ASCE/SEI 7-22. These coefficients, which estimate peak floor accelerations at the design-level earthquake, are modified in this study to consider the intensity of measured ground motions and the level of earthquake-induced inelastic building response. First, the spectral response factors, defined as the ratio between the spectral response acceleration at a given floor and that at the ground, are evaluated at the second- and third-mode periods and compared with those at the first-mode period to assess the higher-mode effects. Then, two metrics are defined to compare the modified acceleration coefficients with the measured peak floor accelerations. The results confirm the need to consider the characteristic dynamics of the buildings to estimate the design forces for floor diaphragms. This consideration is included in ASCE/SEI 7-22 Section 12.10.3 but not rationally considered in Section 12.10.1. The modified acceleration coefficients based on ASCE/SEI 7-22 Section 12.10.1 can considerably underestimate the peak floor accelerations, whereas those based on Section 12.10.3 can capture the increased peak floor accelerations caused by the higher-mode earthquake-induced inertial forces. Thus, the authors recommend using ASCE/SEI 7-22 Section

Department of Structural Engineering, University of California, San Diego, La Jolla, CA, USA

Corresponding author:
C. Franco Mayorga, Department of Structural Engineering, University of California, San Diego, 9500 Gilman Drive, La Jolla, CA 92093, USA.
Email: cfmayorg@ucsd.edu

12.10.3 over Section 12.10.1 to estimate the design forces for floor diaphragms; however, certain assumptions considered in Section 12.10.3 require further revision.

Keywords
Earthquake engineering, seismic design provisions, floor diaphragms, higher-mode effects, instrumented buildings, earthquake strong-motion data

Date received: 2 April 2025; accepted: 30 July 2025

Introduction

Earthquake-resistant buildings

Earthquake-resistant buildings are critical in safeguarding human lives and infrastructure in seismically active regions (Anderson et al., 2010; Belleri et al., 2015; Ghosh and Cleland, 2012; Henry et al., 2017; Iverson and Hawkins, 1994; Saatcioglu et al., 2001). Therefore, the development of seismic design guidelines for earthquake-resistant buildings is of paramount importance to society (ASCE/SEI 7-22, 2021; Kuramoto, 2006; NCh433, 2016; NZS1170.5, 2004). These guidelines have continually evolved to ensure the structural safety and integrity of buildings, aiming to enhance their seismic performance, reliability, and resilience (FEMA P-58, 2018; Panagiotou and Restrepo, 2011; Priestley, 2000; Priestley et al., 2007). The enhancement of the seismic design guidelines has been possible thanks to the continued verification and validation of the assumptions and limitations considered in the design provisions.

The earthquake-resistant buildings typically comprise two systems: (1) the gravity load-resisting system and (2) the seismic force-resisting system (SFRS). The gravity load-resisting system resists the dead, live, and vertical earthquake-induced loads. This system typically consists of horizontal floors and gravity columns. The SFRS resists the horizontal earthquake-induced loads. The vertical elements of this system typically consist of walls, moment frames, braced frames, or a combination of these systems. Some earthquake-resistant buildings consist of only one system simultaneously acting as the gravity load-resisting system and SFRS. Those systems are named bearing systems (ASCE/SEI 7-22, 2021). Figure 1a shows a schematic representation of a reinforced concrete (RC) earthquake-resistant building in which the vertical elements of the SFRS consist of RC moment frames in the global x direction and RC walls in the global y direction. The gravity load-resisting system consists of RC slabs (floors) and columns, both monolithically connected. Most of the seismic mass of a building is distributed on its floor system due to the self-weight of the floors and attached nonstructural components such as equipment, cladding, and partitions.

The gravity and vertical earthquake-induced accelerations on the floors produce vertical loads acting out of the plane of the floors. These loads are primarily transferred from the floors to the gravity columns through gravity beams or directly through out-of-plane internal shear forces in the floors. Each gravity column cumulatively takes the vertical loads corresponding to its tributary area at each floor to the foundations, mainly through axial internal forces. Figure 1a shows the fourth-floor tributary vertical load on one of the interior gravity columns.

The horizontal earthquake-induced accelerations on the floors generate horizontal forces proportional to the seismic mass distributed on the floors. These forces are

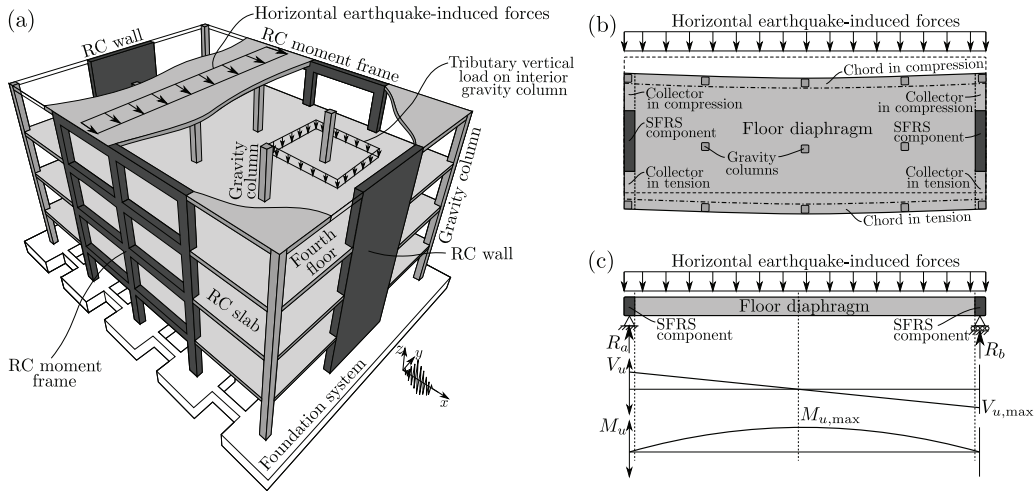


Figure 1. (a) Schematic representation of an earthquake-resistant building. (b) Plan view of the floor diaphragm and its components. (c) Internal shear (V_u), moment (M_u), and reactions at the vertical elements of the SFRS (R_a and R_b).

primarily transferred from the floors to the vertical elements of the SFRS through in-plane internal shear, moment, and collector forces in the floors. The vertical elements of the SFRS take these forces to the foundation through a combination of axial, shear, and moment internal forces.

In addition to transferring vertical and horizontal forces, floors provide the in-plane horizontal kinematic compatibility between the vertical structural elements of the gravity load-resisting system and the vertical elements of the SFRS connected to the same floor. Because of this function, they are known as floor diaphragms. Note that the floor diaphragms form part of both the gravity load-resisting system and SFRS.

Floor diaphragms

Floor diaphragms in their plan view can be conceptually represented by deep beams loaded by distributed horizontal earthquake-induced forces and supported by the laterally stiff structural components of the SFRS, as shown in Figure 1b and c. This beam representation is intended solely to illustrate the internal force mechanisms in floor diaphragms, not as a modeling approach. The internal shear forces (V_u in Figure 1c) generated in the floor diaphragms are resisted by the shear resistance of the cross-section of the floor diaphragms, including distributed reinforcement and/or connectors. The internal moments (M_u in Figure 1c) generated in the floor diaphragms are resisted by the moment resistance provided by the pair of forces from the chords of the floor diaphragms in tension and compression, including localized reinforcement and/or connectors. The collectors are the components of the floor diaphragms that gather the horizontal earthquake-induced forces and transfer them to the vertical elements of the SFRS. These forces transferred through collectors in tension and compression are the reactions (R_a and R_b in Figure 1c) of the beam used to conceptually represent the floor diaphragm. In addition, floor diaphragms resist transfer forces due to in-plane offsets or differences in the lateral stiffness of the vertical elements of the SFRS below and above the floor diaphragms. Floor diaphragms also

resist column bracing forces due to thrusts of inclined columns that are not balanced by other structural elements (Moehle et al., 2016).

Estimates of the horizontal earthquake-induced forces at each floor level of buildings are required for designing the floor diaphragms, including their chords and collectors. These horizontal earthquake-induced forces are proportional to the horizontal earthquake-induced accelerations at each floor level of buildings (Newton's second law).

Past seismic performance of floor diaphragms

Underestimating the horizontal earthquake-induced forces on floor diaphragms could be catastrophic. Loss of the ability of floor diaphragms to transfer forces to the vertical elements of the SFRS could lead to local or total collapse of buildings. Floor diaphragm collapses were observed after the Northridge earthquake due to the loss of connections between floor diaphragms and the vertical elements of precast concrete buildings and tilt-up-wall buildings (Earthquake Spectra, 1996; Fleischman and Farrow, 2001; Iverson and Hawkins, 1994). These types of building systems are generally more vulnerable to horizontal earthquake-induced forces because of the use of non-monolithic connections between the floor diaphragms and the vertical elements of the SFRS. After the 2010–2011 Christchurch earthquakes, excessive damage and collapse of floor diaphragms were attributed to inadequate integrity of the load path, underestimation of horizontal earthquake-induced forces, and poorly understood interactions between floor diaphragms and walls, moment frames, and supporting beams (Gonzalez et al., 2017; Kam et al., 2011; Scarry, 2014). The complex interactions between floor diaphragms and other structural elements result in unpredictable seismic responses, which often lead to unexpected structural damage (Bull, 2004; Henry et al., 2017; Kam et al., 2011; Wallace et al., 2012).

Numerical earthquake simulations of buildings have shown that horizontal earthquake-induced forces on floor diaphragms can greatly exceed their design forces (Rodriguez et al., 2002). These excessive forces can lead to inelastic and potentially non-ductile responses of floor diaphragms (Fleischman et al., 2002; Fleischman and Farrow, 2001). The contribution of the second- and higher-mode responses to the total response of buildings (termed higher-mode effects) can cause excessive floor total accelerations and forces (Chopra, 2007; Sewell et al., 1986). For instance, it has been shown that high floor accelerations due to the higher-mode effects can be expected in buildings with an SFRS that concentrates the inelastic response in a flexural inelastic mechanism at the base, such as buildings with flexure-dominant RC structural walls (Chopra, 2007; Fleischman et al., 2002; López and Cruz, 1996; Panagiotou and Restrepo, 2009; Priestley and Amaris, 2002; Tsampras et al., 2016; Wiebe and Christopoulos, 2009).

Design provisions for floor diaphragms

ASCE/SEI 7-22 Section 12.10.1. ASCE/SEI 7-22 Sections 12.10.1 and 12.10.2 (ASCE/SEI 7-22, 2021) describe a method for estimating the in-plane horizontal earthquake-induced forces that can be used to design floor diaphragms, including their chords and collectors. Section 12.10.1 provides estimates of the horizontal earthquake-induced forces based on the forces used to design the vertical elements of the SFRS. Section 12.10.2 indicates that collectors, and their connections, of buildings assigned to the Seismic Design Categories (SDC) C through F shall be designed for load combinations considering the overstrength of the vertical elements of the SFRS.

Design equations. ASCE/SEI 7-22 Section 12.10.1 indicates that a floor diaphragm shall be designed for both shear and bending stresses resulting from the horizontal earthquake-induced forces estimated as:

$$F_{px}^{(1)} = \frac{\sum_{i=x}^{n} F_i}{\sum_{i=x}^{n} w_i} w_{px} \geqslant 0.2 S_{DS} I_e w_{px} \tag{1}$$

where $F_{px}^{(1)}$ is the floor diaphragm design force at level x; F_i is the design force of the vertical elements of the SFRS applied to level i; w_i is the weight tributary to level i; w_{px} is the weight tributary to the floor diaphragm at level x; S_{DS} is the design, 5% damped, spectral response acceleration parameter at short periods; and I_e is the building importance factor. ASCE/SEI 7-22 Section 12.8.3 indicates that $F_i = C_{vi} V$, where $C_{vi} = w_i h_i^k / \sum_{x=1}^{n} w_x h_x^k$ is the vertical distribution factor; h_i and h_x are the height from the base to levels i and x, respectively; and k is an exponent that depends on the first-mode period of the building. These design provisions consider an upper limit for $F_{px}^{(1)}$ equal to $0.4 S_{DS} I_e w_{px}$. In this study, the design acceleration coefficient at level x per Section 12.10.1 is defined as $C_{px}^{(1)} = F_{px}^{(1)} / w_{px}$ (see Appendix 1 for a complete list of symbols).

Higher-mode response considerations. Although ASCE/SEI 7-22 Commentary C12.8.3 indicates that k is intended to approximate the higher-mode effects, F_i is a fraction of V, which is computed using a seismic response coefficient based on the first-mode period only.

The upper limit of $0.4 S_{DS} I_e$ for F_{px} in Equation 1 is associated with the design ground acceleration, which suggests no acceleration amplification over the height of buildings. This limit contradicts results from both experimental tests and numerical earthquake simulations that show peak floor acceleration amplifications at roof level due to higher-mode effects (Chen et al., 2016; Panagiotou et al., 2011; Rodriguez et al., 2002).

ASCE/SEI 7-22 Section 12.10.3. The alternative design provisions for floor diaphragms per ASCE/SEI 7-22 Section 12.10.3 account for the higher-mode effects and provide estimates of the horizontal earthquake-induced forces, including their chords and collectors. These alternative design provisions are mandatory for precast concrete floor diaphragms in buildings assigned to SDC C through F.

Design equations. The in-plane horizontal earthquake-induced design forces for floor diaphragms, including chords, collectors, and their connections to the vertical elements of the SFRS, are estimated as:

$$F_{px} = \frac{C_{px}^{(3)}}{R_s} w_{px} \geqslant 0.2 S_{DS} I_e w_{px} \tag{2}$$

where $C_{px}^{(3)}$ is the design acceleration coefficient at level x, and R_s is the floor diaphragm design force reduction factor. w_{px}, S_{DS}, and I_e were previously defined. The distribution of $C_{px}^{(3)}$ over the normalized height of buildings is presented in Figure 2. In this figure, N is the number of stories above the base, h_n is the height from the base to the highest level of the SFRS of the building n, $C_{p0}^{(3)}$ is the design acceleration coefficient at the base, $C_{pi}^{(3)}$ is the design acceleration coefficient at $0.8h_n$, and $C_{pn}^{(3)}$ is the design acceleration coefficient at h_n. $C_{p0}^{(3)}$ is equal to $0.4 S_{DS} I_e$ and $C_{pi}^{(3)}$ is calculated as:

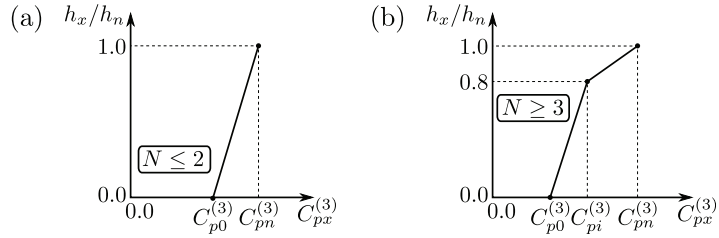


Figure 2. Distribution of $C_{px}^{(3)}$ over the normalized height of buildings with (a) $N \leqslant 2$ and (b) $N \geqslant 3$.

$$C_{pi}^{(3)} = \max\left(0.8C_{p0}^{(3)}, 0.9\Gamma_{m1}\Omega_0 C_s\right) \tag{3}$$

where Ω_0 is the SFRS overstrength factor and C_s is the seismic response coefficient defined in ASCE/SEI 7-22 Section 12.8.1.1. C_s considers the SFRS response modification factor R as a reduction factor. $C_{pn}^{(3)}$ is calculated as:

$$C_{pn}^{(3)} = \sqrt{(\Gamma_{m1}\Omega_0 C_s)^2 + (\Gamma_{m2}C_{s2})^2} \geqslant C_{pi}^{(3)} \tag{4}$$

where $\Gamma_{m1} = 1 + z_s(1 - 1/N)/2$ is the first-mode contribution factor, $\Gamma_{m2} = 0.9z_s(1 - 1/N)^2$ is the higher-mode contribution factor, and:

$$C_{s2} = \begin{cases} \min\left(\frac{I_e S_{D1}}{0.03(N-1)}, (0.15N + 0.25)I_e S_{DS}, I_e S_{DS}\right) & \text{if } N \geqslant 2 \\ 0 & \text{if } N = 1 \end{cases} \tag{5}$$

is the higher-mode seismic response coefficient, which depends on the design, 5% damped, spectral response acceleration parameter at a period of 1 *s*, denoted as S_{D1}. z_s is the mode shape factor defined as 0.3 for buildings designed with buckling restrained braced frame systems, 0.7 for buildings designed with moment-resisting frame systems, 0.85 for buildings designed with dual systems, and 1.0 for buildings designed with any other SFRS.

Mayorga and Tsampras (2022) conducted a simple sensitivity analysis to observe the effects of varying N, R, Ω_0, and z_s on $C_{px}^{(3)}$. It was noted that $C_{px}^{(3)}$ did not considerably change when N increased from 10 to 20. There was a significant reduction in $C_{px}^{(3)}$ when N increased from 20 to 30. $C_{pi}^{(3)}$ was practically invariant and $C_{pn}^{(3)}$ decreased while N increased over 30. $C_{px}^{(3)}$ decreases when R increases and Ω_0 decreases. The relative effects of varying these two parameters are larger on $C_{pi}^{(3)}$ than those on $C_{pn}^{(3)}$ because these parameters only affect the contribution of the first-mode response to the total peak floor accelerations in the formulation of the alternative design provisions. $C_{px}^{(3)}$ decreases when z_s decreases. The effect of varying z_s is lower on $C_{pi}^{(3)}$ than on $C_{pn}^{(3)}$ because z_s has a lower effect on the constant asymptote of Γ_{m1} than on the constant asymptote of Γ_{m2}, affecting more the higher-mode effects in the formulation of the alternative design provisions.

Higher-mode response considerations. ASCE/SEI 7-22 Section 12.10.3.2 neglects the higher-mode effects on $C_{pi}^{(3)}$ by assuming that the second-mode shape is zero at approximately 80% of h_n. ASCE/SEI 7-22 Commentary C12.10.3.2 indicates that $C_{pi}^{(3)}$ is intended to be limited to the lower bound $C_{p0}^{(3)}$, since the higher-mode effects tend to dominate and the contribution of the first-mode response to the peak floor accelerations is minimal at lower floors for systems with high R factors. However, the lower bound considered in

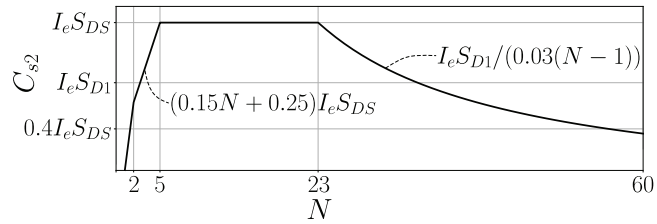


Figure 3. Higher-mode seismic response coefficient in terms of the number of stories.

Equation 3 is actually $0.8C_{p0}^{(3)}$. The higher-mode effects on $C_{pn}^{(3)}$ are included through the term $\Gamma_{m2}C_{s2}$ in Equation 4. The modal contribution factor at roof level, represented by Γ_{m2} for higher modes, is defined as the product of the modal shape ordinate at roof level and the modal participation factor. This definition refers to a concept used in structural dynamics of linear-elastic multistory buildings (Chopra, 2007). The linear-elastic contribution factors are different for flexural-dominant and shear-dominant SFRS because of the difference in the structural dynamic properties of these systems; therefore, although it is not explicitly mentioned in the alternative design provisions and their commentaries, it might be taken into account through the higher-mode contribution factor z_s. However, ASCE/SEI 7-22 Commentary C12.10.3.2 indicates that the difference between low-z_s and high-z_s systems is that the former distributes the inelastic deformations over the height of the building and the latter concentrates them at the base. Therefore, z_s mixes two concepts: (1) the difference in the linear-elastic behavior and (2) the difference in the distribution of inelastic response along the height of buildings with different SFRS. In addition, the commentary does not clearly indicate whether Γ_{m2} considers only the effect of the second mode or the effects of all higher modes.

Figure 3 presents C_{s2} in terms of N, as given in Equation 5. This equation considers that the periods of the higher modes most likely lie on the ascending, constant, or first descending branch of the design response spectrum per ASCE/SEI 7-22 Section 11.4.5.2. Note that buildings with N between 5 and 23 lie on the constant plateau of the design response spectrum.

Remarks. The design equations per ASCE/SEI 7-22 Section 12.10.1 do not consider the higher-mode effects on the magnitude of the floor diaphragm design forces, whereas those per Section 12.10.3 explicitly consider these effects. Thus, the design forces per Section 12.10.3 are expected to provide more accurate estimates of the horizontal earthquake-induced forces than those per Section 12.10.1. However, the alternative design provisions per Section 12.10.3 were developed based on the analysis of limited experimental data from shaking table tests (Chen et al., 2016; Panagiotou et al., 2011) and numerical earthquake simulations (Choi et al., 2008; Fleischman et al., 2013). Therefore, the design provisions for floor diaphragms need to be validated using more extensive data sets, such as the acceleration data and metadata from instrumented buildings subjected to earthquake ground motions.

Scope of study

This article assesses the seismic design provisions for floor diaphragms per ASCE/SEI 7-22 Section 12.10.1 and Section 12.10.3 using strong-motion acceleration data from

instrumented buildings (building stations) monitored by the California Strong Motion Instrumentation Program (CSMIP). The building stations comprise multiple stories and SFRS types.

The spectral response factors at the second- and third-mode periods are compared with those at the first-mode period of the building stations to assess the higher-mode effects on the floor acceleration responses. These factors are defined as the ratio between the spectral response acceleration at a given floor and that at the ground, both evaluated at the same modal period. The periods of the first, second, and third translational modes are estimated from the measured strong-motion data using simplified and analytical expressions provided in the literature. The comparison is used to assess how the higher-mode effects are considered in the design provisions.

The design acceleration coefficients are compared with the peak floor accelerations first computed at the center of rigidity of each instrumented floor and then linearly interpolated to the remaining floors. The center of rigidity location is estimated from the measured strong-motion data using a method described in the literature. Additional acceleration coefficients are introduced as a modified version of the design acceleration coefficients to account for (1) the intensity of the measured ground motions and (2) the level of inelastic response of the building stations induced by the measured ground motions. For these reasons, the modified acceleration coefficients are termed design-based intensity-dependent acceleration coefficients. Two metrics are defined to compare the magnitude and floor-to-ground factor of the design-based intensity-dependent acceleration coefficients with those of the peak floor accelerations over the height of the building stations.

The authors acknowledge that Fourier transform-based methods can be used to assess the higher-mode effects. However, this study explores a spectral response-based method that employs concepts widely used in seismic design of buildings. In addition, this article does not cover the assessment of the transfer forces resisted by the portion of the floor diaphragms between vertical elements of the SFRS, nor the horizontal distribution of the horizontal earthquake-induced forces through the floor diaphragms.

Building stations

The Center for Engineering Strong Motion Data (CESMD) provides raw and processed strong-motion data, along with metadata containing information on measurement stations and measured seismic events, for earthquake engineering applications. The strong-motion data available on the CESMD website are collected at stations in seismic monitoring networks across the United States and worldwide, including the network monitored by the CSMIP. The criteria for the selection of the building stations considered in this study are the following: (1) location of site, (2) seismic risk category, (3) type of SFRS, (4) construction date, (5) number of stories, (6) number of measured ground motions, (7) intensity of measured ground motions, (8) number of measurement channels, (9) spatial distribution of channels, and (10) availability of analyzed data in the literature.

Set of selected building stations

A set of 69 instrumented building stations within the California Geological Survey Network (CE) monitored by the CSMIP was selected. The selected building stations have been subjected to ground motions that induced maximum measured peak channel accelerations of at least $0.2g$ since instrumentation. Figure 4a shows the geographic locations

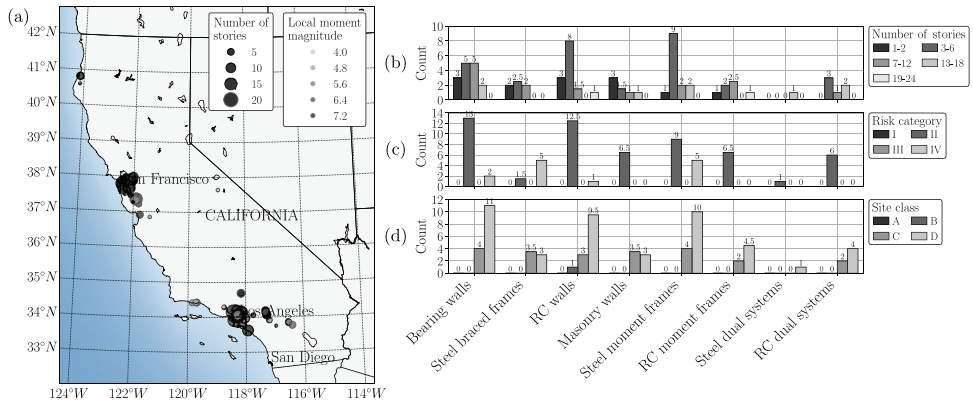


Figure 4. Sixty-nine studied building stations. (a) Geographic location, number of stories, and local moment magnitudes of the ground motions to which the building stations have been subjected. (b) Number of stories, (c) risk category, and (d) site class, each in terms of the SFRS. Half-counting was used for building stations with different SFRS in the two orthogonal directions.

of the selected building stations, with marker size indicating the corresponding number of stories. Most stations are in Los Angeles and San Francisco. The figure also includes a grayscale color map indicating the local moment magnitudes of the ground motions to which the selected building stations have been subjected.

The SFRS for each orthogonal direction of the selected building stations is defined based on the information documented on each building station CESMD website, taking into account the building design date. The SFRS types considered are: bearing walls, steel-braced frames, RC walls, masonry walls, steel moment frames, RC moment frames, steel dual systems, and RC dual systems. The dual systems are SFRS composed of a combination of walls or braced frames and moment frames, where the moment frames can resist at least 25% of the prescribed seismic forces. Figure 4b to d shows the number of stories, risk category, and site class of the building stations by SFRS. The most common SFRS among the selected building stations are bearing walls, RC walls, and steel moment frames, while the least common are steel dual systems, represented by only one building station. The selected building stations have up to 24 stories, fall into the risk categories II or IV, and are located on sites classified as B, C, or D.

Building stations with seismic isolation, stiffness-soft story irregularities, or SFRS not included in ASCE/SEI 7-22 Table 12.2-1 are not considered in the analysis due to their potentially unique distributions of peak floor accelerations over the height (PFA_x, at levels $x = 0, \ldots, n$), compared to those expected for SFRS included in ASCE/SEI 7-22 without structural irregularities.

Framework for analysis of measured strong-motion data and metadata

A workflow for importing, processing, plotting, and utilizing the measured strong-motion data and metadata has been developed using the open-source programming language *Python* (Mayorga and Tsampras, 2025; Van Rossum and Drake, 2009). The workflow consists of 17 steps. The results from each step are stored in the expanded database as

additional metadata. Measured and design-based quantities are introduced and defined progressively within the relevant steps, with design-based quantities explicitly referenced to ASCE/SEI 7-22, where applicable. Each step in the workflow is summarized as follows (see Appendix 2 for a detailed workflow diagram).

Step 1 through Step 5 import, process, and plot the strong-motion data and metadata downloaded from the CESMD website for a selected building station. Additional metadata—such as information from drawings and other sources available for the building station, site, and measured seismic events—are appended to the CESMD metadata.

Step 6 estimates the location of the center of rigidity $\left(x_g^*, y_g^*\right)$ at each sufficiently instrumented floor of the selected building station using the measured strong-motion data. $\left(x_g^*, y_g^*\right)$ is estimated using the method proposed by Şafak and Çelebi (1990) along with the measured strong-motion acceleration time histories of the selected building station (Mayorga and Tsampras, 2022). Step 7 computes and plots the PFA_x at $\left(x_g^*, y_g^*\right)$ for each instrumented floor.

Step 8 computes the 5% damped spectral response accelerations $S_a(T, h_x/h_n)$ and spectral response factors $R_{S_a}(T, h_x/h_n) = S_a(T, h_x/h_n)/S_a(T, h_x/h_n = 0.0)$ at each instrumented floor in the two orthogonal directions of the selected building station for the considered seismic events. Step 9 estimates the first, second, and third translational mode periods (T_i, for $i = 1, 2, 3$) in the two orthogonal horizontal directions of the selected building station using the measured strong-motion data. T_1 is estimated using the empirical equations derived by Xiang et al. (2020). T_2 and T_3 are computed based on the estimated T_1 and the analytical equations for the modal period ratios (T_i/T_1, for $i = 2, 3$) presented by Miranda and Taghavi (2005). Step 10 plots $S_a(T, h_x/h_n)$ and $R_{S_a}(T, h_x/h_n)$ at each instrumented floor.

Step 11 computes and plots the design spectral response accelerations $S_{ad}(T)$ per ASCE/SEI 7-22 Section 12.8, and the 5% damped spectral response accelerations $S_a(T) = S_a(T, h_x/h_n = 0.0)$ at the ground level in the two orthogonal directions of the selected building station. Step 12 computes and plots $C_{px}^{(j)}$, $j = 1, 3$, for $x = 0, \ldots, n$. The superscript j indicates the ASCE/SEI 7-22 section used to compute the design acceleration coefficients ($j = 1$ for Section 12.10.1 and $j = 3$ for Section 12.10.3). The relative vertical distribution of floor seismic weights required to compute $C_{px}^{(1)}$ is estimated based on the relative vertical distribution of floor in-plane areas. Step 13 compares $C_{px}^{(j)}$, $j = 1, 3$ with PFA_x for $x = 0, \ldots, n$; and the floor-to-ground factors $C_{px}^{(j)}/C_{p0}^{(j)}$, $j = 1, 3$ with PFA_x/PGA for $x = 1, \ldots, n$. The measured peak ground acceleration PGA equals PFA_0. It is acknowledged that PFA_x values across the height are induced by seismic events that are not necessarily at the intensity of the design-level ground motion; therefore, $C_{px}^{(j)}$, $j = 1, 3$ need to be adjusted to the intensity of the measured ground motions.

Step 14 estimates the seismic performance factors R and Ω_0 at the intensity of the measured ground motions using the measured strong-motion data. The estimates of the seismic performance factors, denoted as $R_{\delta_{msd}}$ and $\Omega_{0\delta_{msd}}$, are computed based on the peak roof drift δ_{msd} obtained from the measured strong-motion data.

Step 15 computes the floor diaphragm design-based intensity-dependent acceleration coefficients $C_{px,m}^{(j)}$, $j = 1, 3$ across the height for $m = 1, \ldots, 6$. Here, m denotes the approach used to modify $C_{px}^{(j)}$ to account for the intensity of the measured ground motions and the level of inelastic response of the building stations induced by the measured ground motions. Step 16 compares the magnitudes of $C_{px,m}^{(j)}$ with PFA_x, and the floor-to-ground

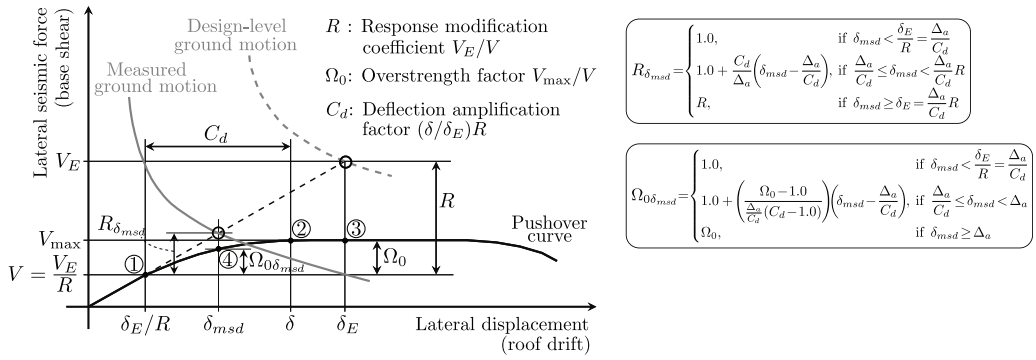


Figure 5. Schematic representation of idealized lateral seismic force versus lateral displacement responses of an earthquake-resistant building. Definition of the seismic performance factors R, Ω_0, and C_d, and the seismic performance factors $R_{\delta_{msd}}$ and $\Omega_{0\delta_{msd}}$ estimated at the intensity of a measured ground motion.

factors $C^{(j)}_{px,m}/C^{(j)}_{p0,m}$ with PFA_x/PGA. Step 17 computes ratio and error metrics to numerically compare these magnitudes and factors.

Design-based intensity-dependent acceleration coefficients

The design acceleration coefficients $C^{(j)}_{px}$, $j = 1, 3$ across the height are modified to account for (1) the intensity of the measured ground motions and (2) the level of inelastic response of the building stations induced by the measured ground motions. The intensity of the measured ground motions is quantified by their spectral response accelerations, while the level of inelastic response of the building stations is quantified by seismic performance factors estimated based on the measured strong-motion data. The modified acceleration coefficients $C^{(j)}_{px,m}$, $j = 1, 3$ across the height are termed design-based intensity-dependent acceleration coefficients, where m is the index identifying the modification approach used to compute them. Six modification approaches are considered in this study; thus, m ranges from 1 to 6.

Seismic performance factors at measured ground motion intensity

The seismic performance factors R and Ω_0 at the intensity of the measured ground motions are determined based on the peak roof drift δ_{msd}, estimated from the strong-motion data. Figure 5 presents the lateral seismic force versus lateral displacement responses for an earthquake-resistant building. The dashed black line represents the base shear versus roof drift response of the building assuming a linear-elastic behavior. The dashed gray curve represents the spectral response acceleration multiplied by the seismic weight versus the spectral response displacement for the design-level ground motion, assuming 5% damping. The intersection of the line and the curve corresponds to the design seismic demand for a linear-elastic single-degree-of-freedom idealization. The solid black curve represents the base shear versus roof drift nonlinear response of the building. The figure illustrates the definition of the seismic performance factors R and Ω_0 used to compute $C^{(j)}_{px}$, $j = 1, 3$. The solid gray curve represents the spectral response acceleration multiplied by the seismic weight versus the spectral response displacement for the measured ground motion. For a measured ground motion with an intensity lower than the design level, the seismic

performance factors $R_{\delta_{msd}}$ and $\Omega_{0\delta_{msd}}$ for a roof drift equal to δ_{msd} (point 4 projection on x-axis) are smaller than the R and Ω_0 expected for the roof drift δ_E associated with the design-level ground motion (point 3 projection on x-axis).

It is assumed that (1) the deformation of the building is dominated by the first-mode translational response and (2) the roof drift δ representing the response of the nonlinear building idealization subjected to the design-level ground motion (point 2 projection on x-axis) is equal to the design upper limit or allowable story drift Δ_a given in ASCE/SEI 7-22 Table 12.12-1 (i.e. $\delta = \Delta_a$, with the story height h_{sx} in the ASCE/SEI 7-22 Table 12.12-1 taken as h_n). Assumption (1) allows the use of the roof drift as a practical global measure of inelastic response, while (2) provides a conservative upper-bound deformation estimate under the premise that the designs of the studied buildings are drift-controlled (i.e. their design is governed by drift rather than strength), making Δ_a a meaningful upper-bound reference for roof drift. As shown in Figure 5, $R_{\delta_{msd}}$ at δ_{msd} (point 4 projection on x-axis) is estimated by linear interpolation between $R_{\delta_{msd}} = 1.0$ at $\delta_{msd} = \delta_E/R = \Delta_a/C_d$ (point 1 projection on x-axis) and $R_{\delta_{msd}} = R$ at $\delta_{msd} = \delta_E = \Delta_a R/C_d$ (point 3 projection on x-axis); and $\Omega_{0\delta_{msd}}$ at δ_{msd} is estimated by linear interpolation between $\Omega_{0\delta_{msd}} = 1.0$ at $\delta_{msd} = \Delta_a/C_d$ (point 1 projection on x-axis) and $\Omega_{0\delta_{msd}} = \Omega_0$ at $\delta_{msd} = \delta = \Delta_a$ (point 2 projection on x-axis). It is considered that $R_{\delta_{msd}} = \Omega_{0\delta_{msd}} = 1.0$ if $\delta_{msd} \leqslant \Delta_a/C_d$, $R_{\delta_{msd}} = R$ if $\delta_{msd} \geqslant \Delta_a R/C_d$, and $\Omega_{0\delta_{msd}} = \Omega_0$ if $\delta_{msd} \geqslant \Delta_a$. R, Ω_0, and C_d are obtained from ASCE/SEI 7-22 Table 12.2-1.

Modification approaches

The design-based intensity-dependent acceleration coefficients are computed as $C^{(j)}_{px,m} = r_{S_a,m} \cdot C^{(j)}_{px}(R_m, \Omega_{0,m})$. Here, $r_{S_a,m}$ is the scaling factor that accounts for the intensity of the measured ground motion, while $C^{(j)}_{px}(R_m, \Omega_{0,m})$ is the design acceleration coefficient expressed as a function of the reduction factor R_m and overstrength factor $\Omega_{0,m}$, which reflect the level of inelastic response of the building stations induced by the measured ground motions. Table 1 summarizes the computation of $r_{S_a,m}$, R_m, and $\Omega_{0,m}$ for $m = 1, \ldots, 6$. For modification approach $m = 6$, the scaling factor $r_{S_a,m}$ is omitted; instead, $C^{(1)}_{px,6}$ is computed as $C^{(1)}_{px}$ using $C_s = S_a(T_1)/R_{\delta_{msd}}$, and $C^{(3)}_{px,6}$ is computed as $C^{(3)}_{px}$ using $C_{p0} = PGA$, $C_s = S_a(T_1)/R_{\delta_{msd}}$, and $C_{s2} = \max(S_a(T_2), S_a(T_3))$.

The first two modification approaches represent the extreme cases in terms of the level of inelastic response of the building stations. The third, fourth, and fifth modification approaches include the level of inelastic response estimated based on the peak roof drift response and use the spectral response accelerations of the ground motions at the first three translational mode periods to compute scaling factors. The sixth modification approach directly incorporates the spectral response accelerations at the first three translational mode periods into the design equations. As a result, $C^{(3)}_{px,m}$ for $m = 6$ takes into account the shape of the acceleration response spectra.

Comparison metrics for assessment of design provisions

The metrics used to compare $C^{(j)}_{px,m}$, $j = 1, 3$, for $m = 1, \ldots, 6$ with PFA_x across the height in terms of their magnitudes and floor-to-ground factors are:

Table 1. Scaling factor $r_{S_a,m}$ reduction factor R_m, and overstrength factor $\Omega_{0,m}$ used to compute $C_{px,m}^{(j)}$ for all modification approaches ($m = 1, \ldots, 6$)

m[a]	j[b]	$r_{S_a,m}$	R_m	$\Omega_{0,m}$
1	1	$r_{S_a}^{1} = S_a(T_1)/S_{ad}(T_1)$	R	–
	3			Ω_0
2	1	$r_{S_a}^{1} = S_a(T_1)/S_{ad}(T_1)$	1.0	–
	3			1.0
3	1	$r_{S_a}^{1} = S_a(T_1)/S_{ad}(T_1)$	$R_{\delta_{msd}}$	–
	3			$\Omega_{0\delta_{msd}}$
4	3	$r_{S_a}^{12} = \sqrt{S_a(T_1)^2 + S_a(T_2)^2}/\sqrt{S_{ad}(T_1)^2 + S_{ad}(T_2)^2}$	$R_{\delta_{msd}}$	$\Omega_{0\delta_{msd}}$
5	3	$r_{S_a}^{123} = \sqrt{S_a(T_1)^2 + S_a(T_2)^2 + S_a(T_3)^2}/\sqrt{S_{ad}(T_1)^2 + S_{ad}(T_2)^2 + S_{ad}(T_3)^2}$	$R_{\delta_{msd}}$	$\Omega_{0\delta_{msd}}$
6	1	–	$R_{\delta_{msd}}$	–
	3			$\Omega_{0\delta_{msd}}$

[a] m indicates the modification approach.
[b] j indicates the section of ASCE/SEI-7 22 to which the modification approach applies.
$j = 1$ for Section 12.10.1 and $j = 3$ for Section 12.10.3.

1. The ratios $r_{\text{mag},x,m}^{(j)} = PFA_x/C_{px,m}^{(j)}$ and $r_{\text{factor},x,m}^{(j)} = (PFA_x/PGA)/\left(C_{px,m}^{(j)}/C_{p0,m}^{(j)}\right)$; and their averages over the building height $\bar{r}_{\text{mag},m}^{(j)} = (1/(n+1)) \times \sum_{x=0}^{n} r_{\text{mag},x,m}^{(j)}$ and $\bar{r}_{\text{factor},m}^{(j)} = (1/(n+1)) \times \sum_{x=0}^{n} r_{\text{factor},x,m}^{(j)}$.
2. The relative errors $e_{\text{mag},x,m}^{(j)} = \left(C_{px,m}^{(j)} - PFA_x\right)/PFA_x$ and $e_{\text{factor},x,m}^{(j)} = \left(C_{px,m}^{(j)}/C_{p0,m}^{(j)} - PFA_x/PGA\right)/(PFA_x/PGA)$; and the average (of their absolute values) over the building height $\bar{e}_{\text{mag},m}^{(j)} = (1/(n+1)) \times \sum_{x=0}^{n} |e_{\text{mag},x,m}^{(j)}|$ and $\bar{e}_{\text{factor},m}^{(j)} = (1/(n+1)) \times \sum_{x=0}^{n} |e_{\text{factor},x,m}^{(j)}|$.

Ratio metrics greater than 1.0 indicate underestimation of the measured responses, while those less than 1.0 indicate overestimation. Error metrics closer to zero indicate a more accurate estimation of the measured responses. Both metrics are selected due to their relative (dimensionless) nature, enabling consistent comparisons across all studied cases.

Assessment of design provisions

This section assesses the floor diaphragm seismic design provisions as per ASCE/SEI 7-22 Section 12.10.1 and Section 12.10.3 using the strong-motion earthquake responses measured by the 69 selected building stations located in California. Emphasis is given to how the design provisions incorporate the higher-mode effects in their formulations. Initially, the floor spectral response accelerations $S_a(T_i, h_x/h_n)$, for $i = 1, 2, 3$ computed from the measured strong-motion data are analyzed. The spectral response factors $R_{S_a}(T_i, h_x/h_n)$, for $i = 1, 2, 3$ are used to study how the spectral response accelerations are amplified or attenuated along the height of the building stations. Subsequently, the design-based intensity-dependent acceleration coefficients $C_{px,m}^{(j)}$, $j = 1, 3$, for $m = 1, \ldots, 6$ are compared with the peak floor accelerations PFA_x computed directly from the measured strong-motion data. The comparison metrics $\bar{r}_{\text{mag},m}^{(j)}$, $\bar{e}_{\text{mag},m}^{(j)}$, $\bar{r}_{\text{factor},m}^{(j)}$, and $\bar{e}_{\text{factor},m}^{(j)}$, $j = 1, 3$, for $m = 1, \ldots, 6$ are

used to numerically quantify the agreement between the magnitudes and floor-to-ground factors of the $C_{px,m}^{(j)}$ and PFA_x across the height. The assessment begins with an example building station, which introduces the computation and interpretation of the variables and metrics used to assess the design provisions. This example building station facilitates a comprehensive understanding of the assessment of the design provisions when extended to multiple building stations with different SFRS.

Note that the quantities presented in this section can be grouped as follows: (1) those computed directly from measured strong-motion data: PFA_x, $S_a(T_i, h_x/h_n)$, and $R_{S_a}(T_i, h_x/h_n)$; (2) those computed from the ASCE/SEI 7-22 seismic design provisions and their intensity-dependent modified versions: $C_{px}^{(j)}$ and $C_{px,m}^{(j)}$; and (3) comparison metrics used to quantify the agreement between design-based and measured results: $\bar{r}_{\text{mag},m}^{(j)}$, $\bar{e}_{\text{mag},m}^{(j)}$, $\bar{r}_{\text{factor},m}^{(j)}$, and $\bar{e}_{\text{factor},m}^{(j)}$. The factors $R_{S_a}(T_i, h_x/h_n)$, for $i = 1, 2, 3$ are used exclusively to assess the higher-mode effects and are not compared directly to design-based quantities. The coefficients $C_{px,m}^{(j)}$, $j = 1, 3$, for $m = 1, \ldots, 6$ are systematically compared with the PFA_x from measured strong-motion data using the comparison metrics listed above.

Example building station

The example building station is a 17-story residential building located in Los Angeles. Its SFRS consists of bearing walls in the two orthogonal directions, its site class is C/D (sedimentary site geology), and its seismic design category is D. This building station was selected because it has been subjected to two ground motions with distinct $S_a(T)$ shapes: one induced by the Landers (1992) seismic event and the other by the Northridge (1994) seismic event. The ratios $S_a(T_2)/S_a(T_1)$ and $S_a(T_3)/S_a(T_1)$ differ between the two selected measured ground motions. One ground motion excites the second and third modes relative to the first mode of the building station more than the other ground motion. The example building station is identified as CE24601 Building Station in the CESMD strong-motion dataset.

Spectral response accelerations. Figure 6a shows the floor spectral response accelerations $S_a(T_i, h_x/h_n)$, for $i = 1, 2, 3$ in the x direction at each instrumented floor of the building station subjected to Landers and Northridge seismic events. For Landers, $S_a(T_1, h_x/h_n = 0.0)$ is marginally larger than $S_a(T_i, h_x/h_n = 0.0)$, for $i = 2, 3$; whereas for Northridge, $S_a(T_1, h_x/h_n = 0.0)$ is lower than $S_a(T_i, h_x/h_n = 0.0)$, for $i = 2, 3$. Figure 6b shows the corresponding spectral response factors $R_{S_a}(T_i, h_x/h_n)$, for $i = 1, 2, 3$ computed for both seismic events. It is observed that $R_{S_a}(T_1, h_x/h_n)$ for both seismic events resembles the typical shape of the first mode. For Landers, $S_a(T_1, h_x/h_n)$ resulted in a $R_{S_a}(T_1, h_x/h_n = 1.0)$ close to 15.0 and $R_{S_a}(T_i, h_x/h_n)$, for $i = 2, 3$ show amplifications of $S_a(T_i, h_x/h_n)$, for $i = 2, 3$. For Northridge, $R_{S_a}(T_i, h_x/h_n)$, for $i = 2, 3$ are lower around $0.7h_n$. Figure 6c presents the ratios $R_{S_a}(T_i, h_x/h_n)/R_{S_a}(T_1, h_x/h_n)$, for $i = 2, 3$ along the height. At the roof level, $R_{S_a}(T_i, h_x/h_n = 1.0)$, for $i = 2, 3$ exceeds 19.0% of $R_{S_a}(T_1, h_x/h_n = 1.0)$ for both seismic events. This result indicates that the contribution of the second- and third-mode responses to the total acceleration response at the roof level is not negligible for this building station.

Peak floor accelerations. Figure 7a to c presents the design and measured spectral response accelerations at the ground, peak floor accelerations, and peak floor acceleration factors, respectively, in the x direction of the building station subjected to the Landers and

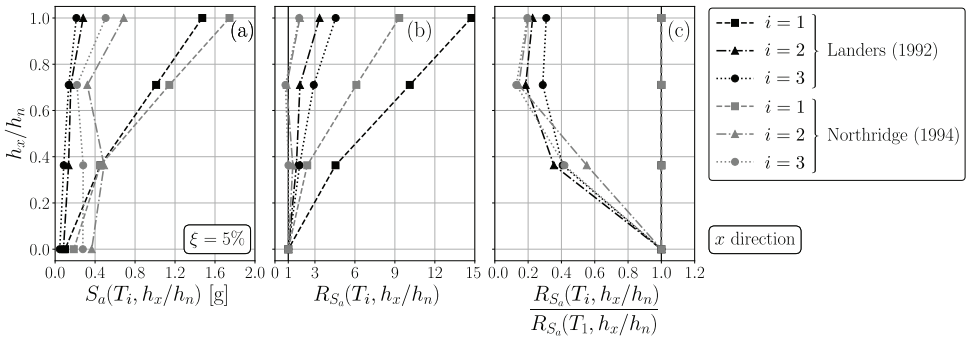


Figure 6. (a) Spectral response accelerations and (b) spectral response factors at T_i, for $i = 1, 2, 3$ computed at instrumented floors. (c) The ratio of the spectral response factors at T_i, for $i = 2, 3$ to the spectral response factor at T_1 computed at instrumented floors. CE24601 Building Station subjected to the Landers (1992) and Northridge (1994) seismic events.

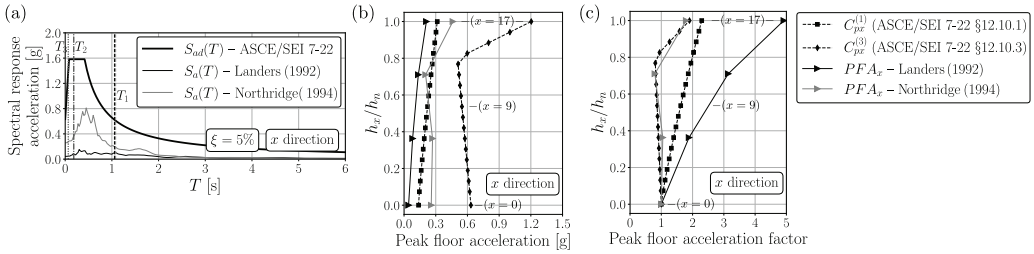


Figure 7. Design and measured (a) spectral response accelerations at the ground, (b) peak floor accelerations, and (c) peak floor acceleration factors of the CE24601 Building Station subjected to the Landers (1992) and Northridge (1994) seismic events.

Northridge seismic events. Figure 7a shows that Landers produced a ground motion with $S_a(T)$ approximately uniform at periods below 2 s, whereas Northridge produced a ground motion with $S_a(T)$ having peak values at periods within $[0.2, 0.7]$ s. Northridge generates $S_a(T)$ closer to $S_{ad}(T)$ compared to $S_a(T)$ for Landers. However, for both seismic events, $S_a(T_i)$, for $i = 1, 2, 3$ are less than one-third of $S_{ad}(T_i)$, for $i = 1, 2, 3$.

Figure 7b shows that $C_{px}^{(3)}$ (per ASCE/SEI 7-22 Section 12.10.3) is never lower than PFA_x across the height for both seismic events. However, $C_{px}^{(1)}$ (per ASCE/SEI 7-22 Section 12.10.1) is lower than PFA_x at most floor levels for Northridge, which is not expected given that the intensity of the measured ground motion is considerably lower than the design level.

Figure 7c shows that $C_{px}^{(3)}/C_{p0}^{(3)}$ more closely matches PFA_x/PGA for Northridge, whereas $C_{px}^{(1)}/C_{p0}^{(1)}$ more closely matches PFA_x/PGA for Landers across all floors. This finding aligns with the observation that $S_a(T_1)$ relative to $S_a(T_2)$ or $S_a(T_3)$ is lower for Northridge than for Landers; thus, the higher-mode response contribution to the total seismic response relative to the first-mode response contribution is expected to be larger for Northridge.

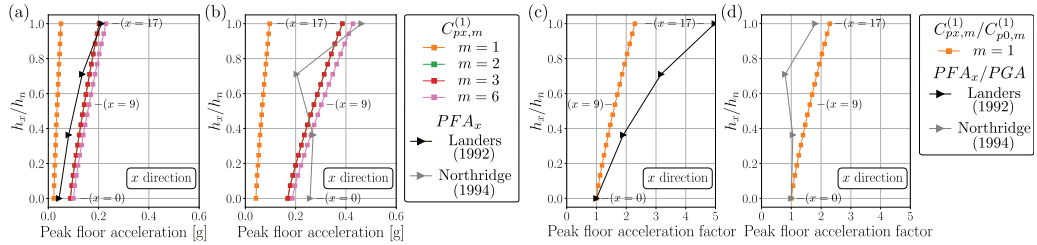


Figure 8. Design-based intensity-dependent and measured peak floor accelerations of the CE24601 Building Station subjected to the (a) Landers (1992) and (b) Northridge (1994) seismic events. Design-based intensity-dependent and measured peak floor acceleration factors for the (c) Landers (1992) and (d) Northridge (1994) seismic events. $C^{(1)}_{px,m}$ based on ASCE/SEI 7-22 Section 12.10.1.

Figure 8a and b shows the design-based intensity-dependent acceleration coefficients ($C^{(1)}_{px,m}$, for $m = 1, 2, 3, 6$) and the peak floor accelerations (PFA_x) in the x direction for Landers and Northridge seismic events, respectively. For both events, $C^{(1)}_{px,1}$ underestimates PFA_x across all floors. The average ratio and error comparison metrics of the $C^{(1)}_{px,1}$ magnitude over the height are $\bar{r}^{(1)}_{\text{mag},1} = 3.02$ and $\bar{e}^{(1)}_{\text{mag},1} = 0.65$ for Landers; and $\bar{r}^{(1)}_{\text{mag},1} = 4.30$ and $\bar{e}^{(1)}_{\text{mag},1} = 0.75$ for Northridge. The values of $C^{(1)}_{px,m}$, for $m = 2, 3$ are the same and thus overlap in the plots, as it is estimated that the building station responded in the linear-elastic range under both seismic events. For both events, $C^{(1)}_{px,3}$ provides a closer estimate of PFA_x on average over the height, with $\bar{r}^{(1)}_{\text{mag},3} = 0.76$ and $\bar{e}^{(1)}_{\text{mag},3} = 0.39$ for Landers; and $\bar{r}^{(1)}_{\text{mag},3} = 1.07$ and $\bar{e}^{(1)}_{\text{mag},3} = 0.21$ for Northridge.

Figure 8c and d presents the design-based intensity-dependent and measured peak floor acceleration factors (floor-to-ground factors). The factors $C^{(1)}_{px,m}/C^{(1)}_{p0,m}$, for $m = 1, 2, 3, 6$ are all equal to $C^{(1)}_{px}/C^{(1)}_{p0}$ across the height, since variations in R and C_s affect only their magnitude. $C^{(1)}_{px,m}/C^{(1)}_{p0,m}$ underestimates PFA_x/PGA for Landers and overestimates PFA_x/PGA for Northridge across all floors. The average ratio and error comparison metrics of the $C^{(1)}_{px,m}/C^{(1)}_{p0,m}$ floor-to-ground factor over the height are $\bar{r}^{(1)}_{\text{factor},m} = 1.54$ and $\bar{e}^{(1)}_{\text{factor},m} = 0.32$ for Landers; and $\bar{r}^{(1)}_{\text{factor},m} = 0.70$ and $\bar{e}^{(1)}_{\text{factor},m} = 0.51$ for Northridge. The lower error for Landers reflects the normalization by the larger PFA_x/PGA values observed for that seismic event.

Figure 9a and b shows the design-based intensity-dependent acceleration coefficients ($C^{(3)}_{px,m}$, for $m = 1, \ldots, 6$) and the peak floor accelerations (PFA_x) in the x direction for Landers and Northridge seismic events, respectively. For both events, $C^{(3)}_{px,6}$ provides the closest match to PFA_x across all floors. The average ratio and error comparison metrics of the $C^{(3)}_{px,6}$ magnitude over the height are $\bar{r}^{(3)}_{\text{mag},6} = 1.08$ and $\bar{e}^{(3)}_{\text{mag},6} = 0.08$ for Landers; and $\bar{r}^{(3)}_{\text{mag},6} = 1.02$ and $\bar{e}^{(3)}_{\text{mag},6} = 0.08$ for Northridge. The values of $C^{(3)}_{px,m}$, for $m = 2, 3$ are also the same and overlap in the plots, as it is estimated that the building station responded in the linear-elastic range under both seismic events.

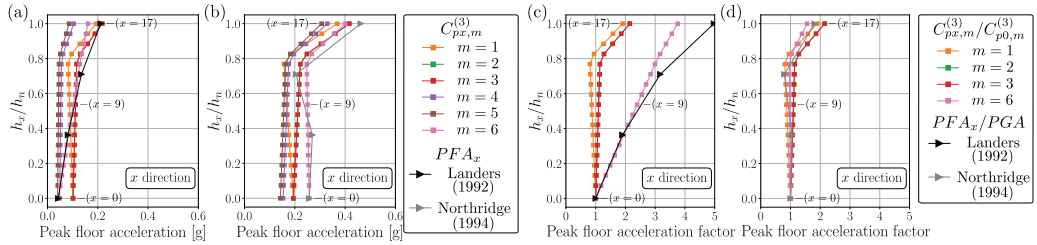


Figure 9. Design-based intensity-dependent and measured peak floor accelerations of the CE24601 Building Station subjected to the (a) Landers (1992) and (b) Northridge (1994) seismic events. Design-based intensity-dependent and measured peak floor acceleration factors for the (c) Landers (1992) and (d) Northridge (1994) seismic events. $C^{(3)}_{px,m}$ based on ASCE/SEI 7-22 Section 12.10.3.

Figure 9c and d presents the design-based intensity-dependent and measured peak floor acceleration factors (floor-to-ground factors). For both seismic events, $C^{(3)}_{px,6}/C^{(3)}_{p0,6}$ provides a closer estimate of PFA_x/PGA on average over the height. The average ratio and error comparison metrics of the $C^{(3)}_{px,6}/C^{(3)}_{p0,6}$ floor-to-ground factor over the height are $\bar{r}^{(3)}_{\text{factor},6} = 1.08$ and $\bar{e}^{(3)}_{\text{factor},6} = 0.08$ for Landers; and $\bar{r}^{(3)}_{\text{factor},6} = 1.02$ and $\bar{e}^{(3)}_{\text{factor},6} = 0.08$ for Northridge. Note that, for $m = 6$, the magnitude and floor-to-ground factor metrics are identical, as $C^{(3)}_{p0,6}$ is defined to be equal to PGA.

It is observed that $C^{(1)}_{px,1}$ can considerably underestimate the PFA_x for seismic events that generate ground motions with spectral response accelerations at the second- and third-mode periods that are large relative to those at the first-mode period. This finding highlights the importance of considering the higher-mode effects when estimating the magnitude of the peak floor accelerations and, therefore, when determining design forces for floor diaphragms. The higher-mode effects are not considered in the magnitude of $C^{(1)}_{px}$, which is the primary alternative for computing the design forces for floor diaphragms given by ASCE/SEI 7-22. Notably, $C^{(3)}_{px,6}$, which explicitly considers the higher-mode effects, can capture both the PFA_x and PFA_x/PGA for seismic events that produce ground motions with different shapes of the acceleration response spectra across the modal periods.

All selected building stations

The floor spectral accelerations and peak floor accelerations computed from the strong-motion data measured by the selected building stations are analyzed statistically. The same quantities and comparison metrics used in the assessment of the design provisions for the example building station are extended to multiple building stations with different SFRS. Building stations with steel dual systems are excluded from the analysis, as only one data point exists for this SFRS among the selected stations.

Spectral response accelerations. Figure 10 presents the mean values of the ratios $R_{S_a}(T_i, h_x/h_n)/R_{S_a}(T_1, h_x/h_n)$, for $i = 2, 3$ computed at normalized heights $h_x/h_n = 0.2, 0.4, 0.6, 0.8$, and 1.0. These mean values are calculated by grouping building stations with the same SFRS, which are shown in separate subplots. The labels of the horizontal axes include a bar above the variable to indicate that they represent mean values. The ratios $R_{S_a}(T_i, h_x/h_n)/R_{S_a}(T_1, h_x/h_n)$, for $i = 2, 3$ are first calculated using the $S_a(T_i, h_x/h_n)$, for $i = 1, 2, 3$ at the instrumented floors of the building stations and then linearly interpolated

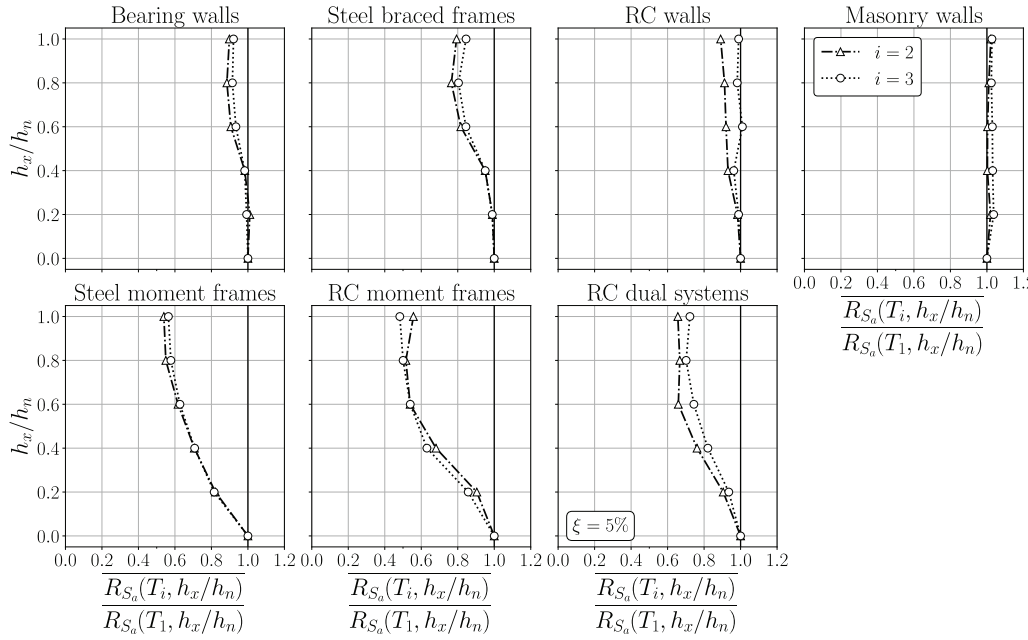


Figure 10. Mean values of the ratio of the spectral response factors at T_i, for $i = 2, 3$ to the spectral response factor at T_1 over the height of the building stations.

at the specified normalized heights. This interpolation is necessary because the instrumented floors of the building stations are located at different normalized heights.

On average, $R_{S_a}(T_i, h_x/h_n)$, for $i = 2, 3$ exceeds 40.0% of $R_{S_a}(T_1, h_x/h_n)$ along the height and across all the SFRS. Except for RC walls and masonry walls, the mean values of the ratios $R_{S_a}(T_i, h_x/h_n)/R_{S_a}(T_1, h_x/h_n)$, for $i = 2, 3$ are closer to 1.0 at bottom levels than at higher levels, where they tend to be lower. The mean values begin to decrease at $h_x/h_n = 0.4$ for bearing walls and $h_x/h_n = 0.2$ for steel-braced frames, while they considerably decrease just above the base level for steel moment frames, RC moment frames, and RC dual systems. The mean values are practically equal to 1.0 over the height for RC walls and masonry walls. It is important to mention that the calculated mean values of the ratios $R_{S_a}(T_i, h_x/h_n)/R_{S_a}(T_1, h_x/h_n)$, for $i = 2, 3$ are associated with considerable dispersion that reflects the variability in the dynamic properties of the building stations with the same SFRS.

Figure 11a presents $R_{S_a}(T_i, h_x/h_n = 1.0)$, for $i = 1, 2, 3$ grouped by SFRS for all selected building stations. The white square markers represent the mean values of the corresponding $R_{S_a}(T_i, h_x/h_n = 1.0)$, for $i = 1, 2, 3$. Most $R_{S_a}(T_i, h_x/h_n = 1.0)$, for $i = 1, 2, 3$ are greater than 1.0, indicating that most of the selected building stations amplified $S_a(T_i, h_x/h_n)$, for $i = 1, 2, 3$ from the ground to the roof when they were subjected to the measured ground motions. Figure 11b shows the ratios $R_{S_a}(T_i, h_x/h_n = 1.0)/R_{S_a}(T_1, h_x/h_n = 1.0)$, for $i = 2, 3$ grouped by SFRS for all selected building stations. The white square markers represent the mean values of the corresponding ratios $R_{S_a}(T_i, h_x/h_n = 1.0)/R_{S_a}(T_1, h_x/h_n = 1.0)$, for $i = 2, 3$. For bearing walls, the ratios $R_{S_a}(T_i, h_x/h_n = 1.0)/R_{S_a}(T_1, h_x/h_n = 1.0)$, for $i = 2, 3$ tend to decrease as N increases; however, this trend is not observed for other SFRS.

Table 2 presents the mean values and coefficients of variation of the ratios $R_{S_a}(T_i, h_x/h_n = 1.0)/R_{S_a}(T_1, h_x/h_n = 1.0)$, for $i = 2, 3$ shown in Figure 11b. The dispersion of

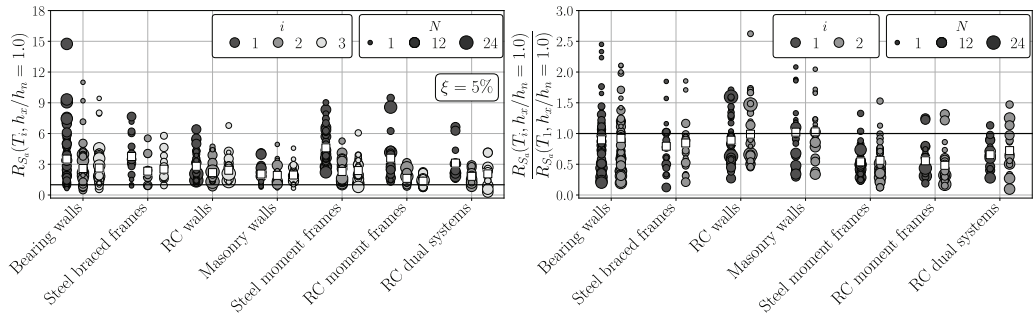


Figure 11. (a) Spectral response factors at T_i, for $i = 1, 2, 3$. (b) The ratio of the spectral response factors at T_i, for $i = 2, 3$ to the spectral response factors at T_1. Spectral response factors computed at roof level ($h_x/h_n = 1.0$).

Table 2. Mean values and coefficients of variation of the spectral response factors at T_i, for $i = 2, 3$ relative to the spectral response factors at T_1 computed at roof level ($h_x/h_n = 1.0$)

SFRS	Count	Mean value μ (coefficient of variation σ/μ (%))	
		$R_{S_a}(T_2, h_x/h_n = 1.0)/R_{S_a}(T_1, h_x/h_n = 1.0)$	$R_{S_a}(T_3, h_x/h_n = 1.0)/R_{S_a}(T_1, h_x/h_n = 1.0)$
Bearing walls	66	0.898 (52.65)	0.921 (46.52)
Steel-braced frames	16	0.793 (61.05)	0.845 (47.55)
RC walls	41	0.891 (28.83)	0.989 (39.73)
Masonry walls	26	1.022 (27.91)	1.027 (31.01)
Steel moment frames	42	0.539 (71.77)	0.564 (83.29)
RC moment frames	21	0.557 (83.29)	0.482 (97.15)
RC dual systems	14	0.656 (34.97)	0.722 (38.61)
All	228	0.787 (54.14)	0.815 (54.21)

these ratios, as indicated by their coefficients of variation, is considerable—particularly for steel moment frames and RC moment frames, for which the coefficients of variation exceed 70%.

The average of the mean values of the ratios $R_{S_a}(T_i, h_x/h_n = 1.0)/R_{S_a}(T_1, h_x/h_n = 1.0)$, for $i = 2, 3$ are approximately 1.0 for masonry walls, 0.95 for RC walls, 0.9 for bearing walls, 0.8 for steel-braced frames, 0.7 for RC dual systems, and 0.5 for steel moment frames and RC moment frames. Differences in these mean values between SFRS can be attributed to variations in the dynamic properties of the selected building stations with different SFRS. These findings are consistent with the formulation of the design equations per ASCE/SEI 7-22 Section 12.10.3, in which the ratio Γ_{m2}/Γ_{m1} for moment frames is lower than that for dual systems, and the ratio for dual systems is lower than that for wall systems with the same N. This distinction among SFRS is controlled by the modal shape factor z_s. The mean values of the ratios $R_{S_a}(T_i, h_x/h_n = 1.0)/R_{S_a}(T_1, h_x/h_n = 1.0)$, for $i = 2, 3$ for steel-braced frames are lower than those for wall systems, indicating differences in the dynamic responses of these SFRS; however, Section 12.10.3 assigns the same z_s to both SFRS. Notably, ASCE/SEI 7-22 Section 12.10.1 does not consider different distributions of the floor diaphragm design forces over the height based on SFRS.

Peak floor accelerations. Figure 12 shows the values of $\bar{r}_{\text{mag}}^{(j)} = (1/(n+1)) \times \sum_{x=0}^{n} PFA_x/C_{px}^{(j)}$, $j = 1, 3$ in terms of SFRS for all selected building stations. These metrics directly compare

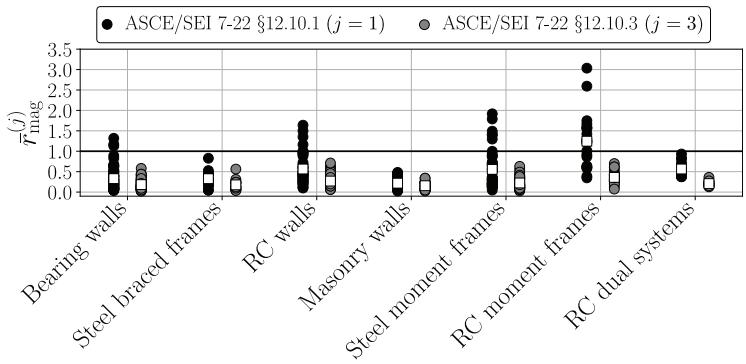


Figure 12. $\bar{r}_{\text{mag}}^{(j)}$, $j = 1, 3$ in terms of the SFRS for each combination of building station and seismic event.

$C_{px}^{(j)}$, $j = 1, 3$ with PFA_x across the height. Each circular marker represents one combination of building station and seismic event in one of the two orthogonal directions (x or y). The black markers correspond to $\bar{r}_{\text{mag}}^{(1)}$ and the gray markers to $\bar{r}_{\text{mag}}^{(3)}$. The white square markers represent the mean values of the corresponding $\bar{r}_{\text{mag}}^{(j)}$, $j = 1, 3$. The figure shows that some of the $\bar{r}_{\text{mag}}^{(1)}$ exceed 1.0, indicating that $C_{px}^{(1)}$ can underestimate PFA_x even if the intensity of the measured ground motions is below the design level. Notably, the mean value of $\bar{r}_{\text{mag}}^{(1)}$ is greater than 1.0 for RC moment frames. In contrast, all $\bar{r}_{\text{mag}}^{(3)}$ are less than 1.0 for every SFRS.

Table 3 presents the mean values and coefficients of variation of $\bar{r}_{\text{mag},m}^{(j)}$, $\bar{e}_{\text{mag},m}^{(j)}$, $\bar{r}_{\text{factor},m}^{(j)}$, and $\bar{e}_{\text{factor},m}^{(j)}$, $j = 1, 3$ considering all the SFRS. The statistics for $\bar{r}_{\text{factor},m}^{(1)}$ and $\bar{e}_{\text{factor},m}^{(1)}$, for $m = 1, 2, 3, 6$ are identical, since $C_{px,m}^{(1)}/C_{p0,m}^{(1)}$, for $m = 1, 2, 3, 6$ are all equal to $C_{px}^{(1)}/C_{p0}^{(1)}$. Similarly, the statistics for $\bar{r}_{\text{factor},m}^{(3)}$ and $\bar{e}_{\text{factor},m}^{(3)}$, for $m = 4, 5$ match those for $m = 3$, as $C_{px,m}^{(3)}/C_{p0,m}^{(3)}$, for $m = 4, 5$ are both equal to $C_{px,3}^{(3)}/C_{p0,3}^{(3)}$. Note also that $C_{px,1}^{(3)}/C_{p0,1}^{(3)}$ equals $C_{px}^{(3)}/C_{p0}^{(3)}$. The table shows that the mean values of $\bar{r}_{\text{mag},m}^{(j)}$, $j = 1, 3$ are in $[0.95, 4.20]$, with coefficients of variation up to 141.5%. The mean values of $\bar{e}_{\text{mag},m}^{(j)}$, $j = 1, 3$ reach up to 1.08, with coefficients of variation in $[43.1, 95.8]$%. The mean values of $\bar{r}_{\text{factor},m}^{(j)}$, $j = 1, 3$ are in $[0.98, 1.22]$, with coefficients of variation no greater than 40.2%. The mean values of $\bar{e}_{\text{factor},m}^{(j)}$, $j = 1, 3$ are no greater than 0.37, with coefficients of variation in $[84.3, 110.7]$%. These results show that the accuracy and consistency of estimating the factors PFA_x/PGA are notably superior to those of estimating the magnitude of PFA_x across the height of the building stations.

Table 3 shows that, for $\bar{r}_{\text{mag},m}^{(1)}$, the mean value closest to 1.0 is obtained for $m = 3$ (0.98), while the lowest coefficient of variation is obtained for $m = 6$ (112.2%). For $\bar{r}_{\text{mag},m}^{(3)}$, both the mean value closest to 1.0 (1.04) and the lowest coefficient of variation (35.8%) are obtained for $m = 6$. Regarding the error metrics, the mean values of $\bar{e}_{\text{mag},m}^{(1)}$, for $m = 2, 3, 6$ are more than twice those of $\bar{e}_{\text{mag},m}^{(3)}$ for the corresponding m values. The lowest mean value of $\bar{e}_{\text{mag},m}^{(1)}$ is 0.59 for $m = 1$, with a coefficient of variation of 43.1%, whereas the lowest mean value of $\bar{e}_{\text{mag},m}^{(3)}$ is 0.32 for $m = 6$, with a coefficient of variation of 95.8%. Note that, although the

Table 3. Mean values and coefficients of variation of $\bar{r}^{(j)}_{\text{mag},m}$, $\bar{e}^{(j)}_{\text{mag},m}$, $\bar{r}^{(j)}_{\text{factor},m}$, and $\bar{e}^{(j)}_{\text{factor},m}$, $j = 1, 3$ considering all the SFRS

m	Mean value μ (coefficient of variation σ/μ (%))							
	$\bar{r}^{(1)}_{\text{mag},m}$	$\bar{r}^{(3)}_{\text{mag},m}$	$\bar{e}^{(1)}_{\text{mag},m}$	$\bar{e}^{(3)}_{\text{mag},m}$	$\bar{r}^{(1)}_{\text{factor},m}$	$\bar{r}^{(3)}_{\text{factor},m}$	$\bar{e}^{(1)}_{\text{factor},m}$	$\bar{e}^{(3)}_{\text{factor},m}$
1	4.20 (141.5)	1.75 (97.7)	0.59 (43.1)	0.48 (75.0)	1.04 (32.9)	1.22 (40.2)	0.25 (110.7)	0.32 (101.4)
2	0.96 (121.5)	1.42 (100.9)	1.08 (89.3)	0.47 (78.6)	1.04 (32.9)	0.98 (36.4)	0.25 (110.7)	0.37 (84.7)
3	0.98 (119.7)	1.42 (100.5)	1.07 (91.6)	0.47 (79.5)	1.04 (32.9)	0.99 (36.6)	0.25 (110.7)	0.36 (84.3)
4	– (–)	1.13 (46.3)	– (–)	0.38 (70.5)	– (–)	0.99 (36.6)	– (–)	0.36 (84.3)
5	– (–)	1.14 (44.6)	– (–)	0.37 (67.1)	– (–)	0.99 (36.6)	– (–)	0.36 (84.3)
6	0.95 (112.2)	1.04 (35.8)	1.00 (87.0)	0.32 (95.8)	1.04 (32.9)	1.00 (32.7)	0.25 (110.7)	0.31 (95.4)

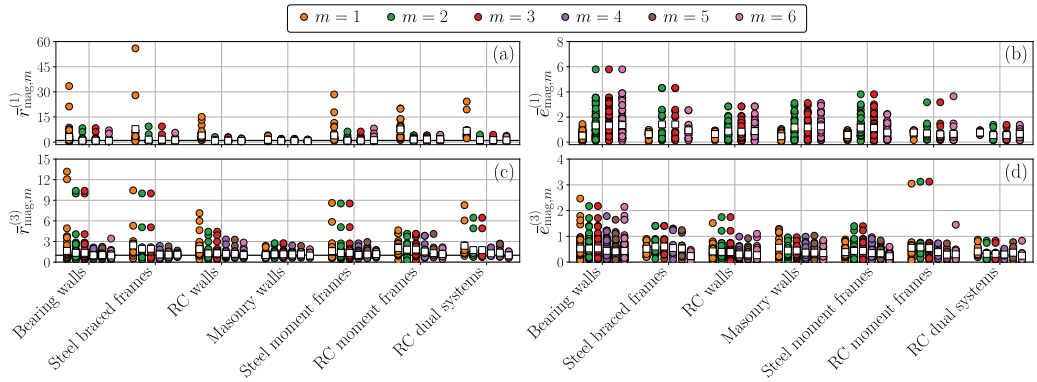


Figure 13. (a) $\bar{r}^{(1)}_{\text{mag},m}$, (b) $\bar{e}^{(1)}_{\text{mag},m}$ (c) $\bar{r}^{(3)}_{\text{mag},m}$, and (d) $\bar{e}^{(3)}_{\text{mag},m}$, for $m = 1, \ldots, 6$ comparison metrics in terms of the SFRS for each combination of building station and seismic event.

coefficient of variation of $\bar{e}^{(1)}_{\text{mag},1}$ is less than half that for $\bar{e}^{(3)}_{\text{mag},6}$, their standard deviation is similar, since the mean value of $\bar{e}^{(1)}_{\text{mag},1}$ is approximately twice that of $\bar{e}^{(3)}_{\text{mag},6}$.

Table 3 indicates that the mean values of $\bar{r}^{(1)}_{\text{factor},m}$, for $m = 1, 2, 3, 6$ are all equal to 1.04, with coefficients of variation equal to 32.9%. For $\bar{r}^{(3)}_{\text{factor},m}$, the mean value closest to 1.0 (1.00) and the lowest coefficient of variation (32.7%) are both obtained for $m = 6$. The mean values and coefficients of variation of $\bar{e}^{(1)}_{\text{factor},m}$ and $\bar{e}^{(3)}_{\text{factor},m}$ are comparable for $m = 2, 3, 6$, with differences not exceeding 48% for mean values and 24% for coefficients of variation. Thus, $C^{(3)}_{px,6}$ is observed to result in combinations of ratio metrics closest to 1.0, with the lowest coefficient of variation and the lowest error metrics among all design-based intensity-dependent acceleration coefficients across all the SFRS.

Figure 13a and b shows the comparison metrics $\bar{r}^{(1)}_{\text{mag},m}$ and $\bar{e}^{(1)}_{\text{mag},m}$, respectively, for $m = 1, \ldots, 6$. Figure 13c and d shows the comparison metrics $\bar{r}^{(3)}_{\text{mag},m}$ and $\bar{e}^{(3)}_{\text{mag},m}$,

respectively, for $m = 1, \ldots, 6$. All comparison metrics are presented in terms of the SFRS for all selected building stations. Each colored circular marker represents one combination of building station and seismic event in one of the two orthogonal directions (x or y). The white square markers represent the mean values of the corresponding comparison metrics.

Table 4 presents the mean values and coefficients of variation of $\bar{r}^{(j)}_{\text{mag},m}$, $j = 1, 3$ shown in Figure 13a and c. Table 5 presents the mean values and coefficients of variation of $\bar{e}^{(j)}_{\text{mag},m}$, $j = 1, 3$ shown in Figure 13b and d. For direct comparison, results based on ASCE/SEI 7-22 Sections 12.10.1 and 12.10.3 are presented in adjacent columns. The tables also report the count of combinations of building stations and seismic events, with each of the two orthogonal directions (x or y) considered as an independent data point.

Figure 13a and c illustrates considerable dispersion in $\bar{r}^{(1)}_{\text{mag},m}$ and $\bar{r}^{(3)}_{\text{mag},m}$, $m = 1, \ldots, 6$, indicating substantial variability in these comparison metrics across building stations and seismic events. Table 4 shows that the dispersion in terms of coefficient of variation is highest for $\bar{r}^{(1)}_{\text{mag},1}$ across all the SFRS. This comparison metric exhibits values exceeding 25 for systems such as bearing walls, steel braced frames, and steel moment frames. These results demonstrate that $C^{(1)}_{px,1}$ can considerably underestimate PFA_x.

Effects of level of nonlinear response. Table 4 shows that, except for masonry walls, the mean values of $\bar{r}^{(j)}_{\text{mag},3}$, $j = 1, 3$ are closer to 1.0 than those of $\bar{r}^{(j)}_{\text{mag},1}$, $j = 1, 3$, respectively. For all the SFRS, the coefficients of variation of $\bar{r}^{(j)}_{\text{mag},3}$, $j = 1, 3$ are close to those of $\bar{r}^{(1)}_{\text{mag},1}$, $j = 1, 3$, respectively, with differences not exceeding 25%. Table 5 shows that the mean values and coefficients of variation of $\bar{e}^{(1)}_{\text{mag},3}$ are higher than those of $\bar{e}^{(1)}_{\text{mag},1}$ for all the SFRS, while the mean values and coefficients of variation of $\bar{e}^{(3)}_{\text{mag},3}$ are close to those of $\bar{e}^{(3)}_{\text{mag},1}$, with differences not exceeding 22% for the mean values and 44% for the coefficients of variation. Figure 13 further shows that almost all $\bar{r}^{(j)}_{\text{mag},3}$ and $\bar{e}^{(j)}_{\text{mag},3}$, $j = 1, 3$ coincide with those of $\bar{r}^{(j)}_{\text{mag},2}$ and $\bar{e}^{(j)}_{\text{mag},3}$, $j = 1, 3$, respectively, which is reflected in the statistics presented in Tables 4 and 5. This outcome is attributed to the fact that most of the measured ground motions were considerably lower in intensity compared to the design level. Consequently, it was estimated that the building station responses were in or near the linear-elastic range ($R_{\delta_{msd}} \approx 1.0$ and $\Omega_{0\delta_{msd}} \approx 1.0$). Therefore, the lack of building stations subjected to ground motions with intensities close to the design level does not allow us to draw conclusions about the effects of the estimation of the level of nonlinearity to which the building stations were subjected on the capability of $C^{(j)}_{px,m}$, $j = 1, 3$ to estimate PFA_x.

Effect of including $S_a(T_2)$ and $S_a(T_3)$ in scaling factors. Table 4 shows that the mean values of $\bar{r}^{(3)}_{\text{mag},m}$, for $m = 4, 5$ are closer to 1.0 than those for $m = 3$. In addition, the coefficients of variation of $\bar{r}^{(3)}_{\text{mag},m}$, for $m = 4, 5$ are lower than those for $m = 3$, being less than half for bearing walls and steel moment frames. Table 5 shows that the mean values of $\bar{e}^{(3)}_{\text{mag},m}$, for $m = 4, 5$ are lower than those for $m = 3$. Except for RC moment frames, the coefficients of variation of $\bar{e}^{(3)}_{\text{mag},m}$, for $m = 4, 5$ are close to those for $m = 3$, with differences not exceeding 34%. For RC moment frames, the coefficient of variation of $\bar{e}^{(3)}_{\text{mag},4}$ is more than 50% lower than that for $m = 3$. These results demonstrate that using $r^{12}_{S_a}$ or $r^{123}_{S_a}$ instead of $r^{1}_{S_{a1}}$ (all as defined in Table 1) as a scaling factor improves the capability of $C^{(3)}_{px,m}$ to estimate PFA_x.

Table 4. Mean values and coefficients of variation of the $\bar{r}^{(j)}_{\text{mag},m}$, $j = 1, 3$ ratios

SFRS	Count	Mean value $\mu_{\bar{r}^{(j)}_{\text{mag},m}}$ (coefficient of variation $\sigma_{\bar{r}^{(j)}_{\text{mag},m}}/\mu_{\bar{r}^{(j)}_{\text{mag},m}}$ (%))											
		$m = 1$[a]		$m = 2$		$m = 3$		$m = 4$		$m = 5$		$m = 6$	
		$j = 1$[b]	$j = 3$	$j = 1$	$j = 3$	$j = 1$	$j = 3$	$j = 1$	$j = 3$	$j = 1$	$j = 3$	$j = 1$	$j = 3$
Bearing walls	66	3.05 (158.3)	1.64 (131.3)	0.86 (143.7)	1.35 (126.0)	0.86 (143.7)	1.35 (126.0)	– (–)	1.00 (39.2)	– (–)	1.02 (40.8)	0.78 (133.7)	0.96 (44.4)
Steel-braced frames	16	7.81 (184.3)	2.43 (100.9)	1.46 (161.4)	1.94 (125.2)	1.46 (161.4)	1.94 (125.2)	– (–)	1.11 (51.9)	– (–)	1.09 (51.2)	1.11 (122.3)	1.08 (27.1)
RC walls	41	3.92 (74.0)	1.89 (69.3)	0.79 (72.5)	1.27 (64.3)	0.81 (71.0)	1.27 (63.8)	– (–)	1.20 (40.5)	– (–)	1.20 (38.4)	0.72 (58.6)	1.04 (39.1)
Masonry walls	26	1.39 (65.7)	1.03 (46.2)	0.70 (65.7)	1.15 (48.0)	0.70 (65.7)	1.15 (48.0)	– (–)	1.11 (36.1)	– (–)	1.12 (34.6)	0.60 (55.7)	0.96 (31.6)
Steel moment frames	42	4.01 (124.4)	1.60 (88.2)	0.89 (124.4)	1.33 (104.3)	0.91 (121.4)	1.34 (103.7)	– (–)	1.04 (45.9)	– (–)	1.12 (46.1)	1.17 (122.6)	1.17 (24.6)
RC moment frames	21	7.59 (72.3)	2.05 (56.3)	1.52 (72.3)	1.81 (60.8)	1.60 (65.9)	1.83 (59.4)	– (–)	1.54 (58.3)	– (–)	1.31 (56.3)	1.67 (71.7)	1.18 (35.9)
RC dual systems	14	6.72 (98.4)	2.37 (89.4)	1.22 (98.4)	1.76 (97.8)	1.22 (98.4)	1.76 (97.8)	– (–)	1.28 (35.3)	– (–)	1.37 (49.1)	1.09 (96.5)	0.99 (27.7)

[a] m indicates the modification approach.
[b] j indicates the section of ASCE/SEI-7 22 to which the modification approach applies. $j = 1$ for Section 12.10.1 and $j = 3$ for Section 12.10.3.

Table 5. Mean values and coefficients of variation of the $\bar{e}^{(j)}_{mag,m}$, $j = 1, 3$ errors

SFRS	Count	Mean value $\mu_{\bar{e}^{(j)}_{mag,m}}$ (coefficient of variation $\sigma_{\bar{e}^{(j)}_{mag,m}}/\mu_{\bar{e}^{(j)}_{mag,m}}$ (%))											
		$m = 1$[a]		$m = 2$		$m = 3$		$m = 4$		$m = 5$		$m = 6$	
		$j = 1$[b]	$j = 3$	$j = 1$	$j = 3$	$j = 1$	$j = 3$	$j = 1$	$j = 3$	$j = 1$	$j = 3$	$j = 1$	$j = 3$
Bearing walls	66	0.51 (58.3)	0.53 (80.0)	1.32 (85.3)	0.53 (74.0)	1.32 (85.3)	0.53 (74.0)	– (–)	0.44 (74.9)	– (–)	0.42 (72.4)	1.35 (81.0)	0.43 (100.4)
Steel-braced frames	16	0.64 (38.7)	0.52 (48.3)	1.41 (98.8)	0.60 (62.7)	1.41 (98.8)	0.60 (62.7)	– (–)	0.55 (71.4)	– (–)	0.53 (67.8)	0.94 (77.6)	0.23 (53.4)
RC walls	41	0.64 (27.8)	0.42 (63.4)	0.85 (84.3)	0.40 (79.6)	0.83 (87.6)	0.39 (81.2)	– (–)	0.30 (58.7)	– (–)	0.30 (53.7)	0.88 (81.2)	0.27 (88.1)
Masonry walls	26	0.47 (58.6)	0.56 (64.3)	1.17 (80.4)	0.45 (54.1)	1.17 (80.4)	0.45 (54.1)	– (–)	0.37 (66.8)	– (–)	0.37 (66.3)	1.25 (73.5)	0.35 (73.6)
Steel moment frames	42	0.57 (37.4)	0.39 (50.9)	1.15 (74.6)	0.43 (73.4)	1.12 (78.9)	0.44 (73.4)	– (–)	0.35 (66.1)	– (–)	0.34 (52.8)	0.76 (74.2)	0.23 (58.1)
RC moment frames	21	0.76 (25.2)	0.55 (110.4)	0.70 (96.9)	0.57 (107.8)	0.62 (108.0)	0.55 (114.1)	– (–)	0.39 (51.0)	– (–)	0.29 (60.9)	0.66 (117.1)	0.30 (97.1)
RC dual systems	14	0.76 (14.4)	0.41 (52.6)	0.56 (66.2)	0.32 (71.0)	0.56 (66.2)	0.32 (71.0)	– (–)	0.30 (46.8)	– (–)	0.36 (52.5)	0.66 (61.2)	0.25 (82.2)

[a] m indicates the modification approach.

[b] j indicates the section of ASCE/SEI-7 22 to which the modification approach applies. $j = 1$ for Section 12.10.1 and $j = 3$ for Section 12.10.3.

This observation suggests that $r_{S_a}^{12}$ or $r_{S_a}^{123}$ could be considered as ground motion intensity measures for floor acceleration responses.

Effects of $S_a(T)$ shape. The shapes of the acceleration response spectra are considered in $C_{px,6}^{(3)}$, as the modification approach $m=6$ directly includes $S_a(T_i)$, for $i=1,2,3$, to modify the design equations per ASCE/SEI 7-22 Section 12.10.3. $C_{px,6}^{(3)}$ is compared with $C_{px,5}^{(3)}$, which also considers $S_a(T_i)$, for $i=1,2,3$; however, the modification approach $m=5$ only uses these values to compute the scaling factor given in Table 1. Table 4 shows that, except for bearing walls and steel moment frames, the mean values of $\bar{r}_{\text{mag},6}^{(3)}$ are closer to 1.0 than those of $\bar{r}_{\text{mag},5}^{(3)}$. For bearing walls and steel moment frames, the differences between the mean values for $m=6$ and $m=5$ are less than 6%. The coefficients of variation of $\bar{r}_{\text{mag},6}^{(3)}$ are more than 35% lower than those of $\bar{r}_{\text{mag},5}^{(3)}$ for steel braced frames, steel moment frames, RC moment frames, and RC dual systems, while for the remaining SFRS, the coefficients of variation for $m=6$ are less than 10% larger than those for $m=5$. Table 5 shows that, for most of the SFRS, the mean values of $\bar{e}_{\text{mag},6}^{(3)}$ are lower than those of $\bar{e}_{\text{mag},5}^{(3)}$, being only less than 4% larger for bearing walls and RC moment frames. Except for steel braced frames, the coefficients of variation of $\bar{e}_{\text{mag},6}^{(3)}$ are larger than those of $\bar{e}_{\text{mag},5}^{(3)}$, with differences up to 64% for RC walls. Despite the higher coefficients of variation in the error metrics, it is considered that including the $S_a(T)$ shape in the formulation of modification approach $m=6$ generally improves the capability of $C_{px,m}^{(3)}$ to estimate PFA_x.

Effects of SFRS. The seven SFRS are compared for $C_{px,6}^{(3)}$ only, since the previous analysis of the comparison metrics suggests that this design-based intensity-dependent acceleration coefficient generally provides more accurate estimates of PFA_x than the other coefficients considered in the study. Tables 4 and 5 show that $C_{px,6}^{(3)}$ provides the best estimates of PFA_x for RC dual systems, with a mean value of $\bar{r}_{\text{mag},6}^{(3)}$ equal to 0.99, a coefficient of variation of 27.7%, and a mean value of $\bar{e}_{\text{mag},6}^{(3)}$ equal to 0.25. Conversely, $C_{px,6}^{(3)}$ provides the least accurate estimates of PFA_x for RC moment frames, with a mean value of $\bar{r}_{\text{mag},6}^{(3)}$ equal to 1.18, a coefficient of variation of 35.9%, and a mean value of $\bar{e}_{\text{mag},6}^{(3)}$ equal to 0.30, although it still represents a reasonable approximation.

Conclusion

This article assessed the seismic design provisions for floor diaphragms per ASCE/SEI 7-22 Section 12.10.1 and Section 12.10.3, focusing on how these provisions consider the higher-mode effects on the horizontal floor accelerations of earthquake-resistant buildings. While the design provisions were developed based on limited experimental tests and numerical earthquake simulations, this study assesses these provisions using strong-motion data from a diverse set of instrumented buildings in California. In addition, the framework developed for processing and analyzing the strong-motion data provides a practical tool that can facilitate the use of the CSMIP data set in other research and engineering applications. Based on the results of this study, the following conclusions can be drawn:

- The mean values of the ratio of the spectral response factors at the second- and third-mode periods to those at the first-mode period, computed at roof level, are lower for steel moment frames and RC moment frames than for wall systems. This result is consistent with the formulation of the design equations per ASCE/SEI 7-22 Section 12.10.3. However, the dispersion of these results is considerable, especially for steel moment frames and RC moment frames.

- The mean values of the ratio of the spectral response factors at the second- and third-mode periods to those at the first-mode period, computed at roof level, are lower for steel braced frames than for wall systems. However, ASCE/SEI 7-22 Section 12.10.3 assigns the same mode shape factor to these SFRS.
- The design-based intensity-dependent acceleration coefficients based on ASCE/SEI 7-22 Section 12.10.1 can significantly underestimate the peak floor accelerations if the spectral response accelerations at the ground evaluated at the second- and third-mode periods are considerably larger compared to those evaluated at the first-mode period.
- The design-based intensity-dependent acceleration coefficients based on ASCE/SEI 7-22 Section 12.10.3 can capture the increase of peak floor accelerations caused by either the higher-mode spectral response accelerations at the ground or by the higher-mode response contribution characteristic of the dynamic properties of the building stations.

Data from instrumented buildings subjected to design-level ground motions and multi-directional earthquake simulation tests are needed to fully validate floor diaphragm design provisions. Increasing the number of instrumented floors of building stations based on the number of stories will improve the assessment of higher-mode effects, particularly at mid-height levels of buildings.

The authors recommend using the alternative design provisions per ASCE/SEI 7-22 Section 12.10.3 over Section 12.10.1 to estimate the seismic-induced horizontal inertial forces for floor diaphragm design. However, the definition of the mode shape factor given in Section 12.10.3 needs to be revised to clarify the distinction between the effects of linear-elastic dynamics and the distribution of nonlinearity over the height of the building on the peak floor acceleration responses of different SFRS.

Authors' note

Any opinions, findings, and conclusions expressed in this paper are those of the authors and do not necessarily reflect the views of others acknowledged here.

Acknowledgments

The authors thank Dr. Daniel Swensen for coordinating the project activities, and Dr. Lisa Schleicher, Dr. Mehmet Çelebi, and Dr. Erdal Şafak for their assistance in implementing the method to estimate the location of the center of rigidity of the building stations from measured data. The inputs from the members of the Buildings and Data Utilization Strong Motion Instrumentation Advisory Subcommittees are also gratefully acknowledged.

ORCID iDs

C Franco Mayorga https://orcid.org/0009-0009-2471-5207
Georgios Tsampras https://orcid.org/0000-0001-8255-3415

Funding

The authors disclosed receipt of the following financial support for the research, authorship, and/or publication of this article. This research was supported by the California Strong Motion Instrumentation Program through the project "Validation of Seismic Design Provisions for Diaphragms and Assessment of Higher-Mode Responses on Earthquake-Resistant Buildings," and by the Chilean National Agency for Research and Development (ANID) through the Foreign Doctoral Scholarship 2020.

Declaration of conflicting interests

The authors declared no potential conflicts of interest with respect to the research, authorship, and/or publication of this article.

Data and resources

The framework developed in this study for processing and utilizing data from the CESMD to assess seismic design provisions for floor diaphragms is publicly available on DesignSafe-CI (Mayorga and Tsampras, 2025). This framework enables the reproducibility of the results of this study and facilitates further research on the topic.

References

Anderson R, Angel J, Callister J, Creveling M, Edwards C, Everingham L, Garcia-Delgado V, Gastelum A, Guerrini G, Hernandez R, Hoehler M, Meneses J, Hutchinson T, King D, Koutromanos I, Mathieson B, Mazzoni S, McGavin G and Mosele F (2010) The El Mayor Cucapah, Baja California earthquake April 4, 2010: An EERI Learning from Earthquakes Reconnaissance Report. Oakland, CA: Earthquake Engineering Research Institute. EERI Publication Number: 2010-02. Available at: https://learningfromearthquakes.org/resources/the-el-mayor-cucapah-baja-california-earthquake-reconnaissance-report/ (accessed September 29, 2025).

ASCE/SEI 7-22 (2021) *Minimum Design Loads and Associated Criteria for Buildings and Other Structures*. Reston, VA: American Society of Civil Engineers.

Belleri A, Brunesi E, Nascimbene R, Pagani M and Riva P (2015) Seismic performance of precast industrial facilities following major earthquakes in the Italian territory. *Journal of Performance of Constructed Facilities* 29: 04014135.

Bull DK (2004) Understanding the complexities of designing diaphragms in buildings for earthquakes. *Bulletin of the New Zealand Society for Earthquake Engineering* 37: 70–88.

CESMD website (n.d.) Center for Engineering Strong Motion Data website. Available at: https://www.strongmotioncenter.org/ (accessed September 29, 2025).

Chen MC, Pantoli E, Wang X, Astroza R, Ebrahimian H, Hutchinson TC, Conte JP, Restrepo JI, Marin C, Walsh KD, Bachman RE, Hoehler MS, Englekirk R and Faghihi M (2016) Full-scale structural and nonstructural building system performance during earthquakes: Part I—Specimen Description, Test Protocol, and Structural Response. *Earthquake Spectra* 32: 737–770.

Choi H, Erochko J, Christopoulos C and Tremblay R (2008) Comparison of the seismic response of steel buildings incorporating self-centering energy dissipative braces, buckling. In: *The 14th world conference on earthquake engineering*, Beijing, China, 12–17 October.

Chopra AK (2007) *Dynamics of Structures*. London: Pearson Education.

Earthquake Spectra (1996) Tilt-up-wall buildings. Earthquake Spectra 12: 99–123.

FEMA P-58 (2018) *Seismic performance assessment of buildings, Volume 1—methodology, Second Edition*. Tech. Rep. FEMA P-58-1. Washington, DC: Federal Emergency Management Agency.

Fleischman RB and Farrow KT (2001) Dynamic behavior of perimeter lateral-system structures with flexible diaphragms. *Earthquake Engineering & Structural Dynamics* 30: 745–763.

Fleischman RB, Farrow KT and Eastman K (2002) Seismic performance of perimeter lateral-system structures with highly flexible diaphragms. *Earthquake Spectra* 18: 251–286.

Fleischman RB, Restrepo JI, Naito CJ, Sause R, Zhang D and Schoettler M (2013) Integrated analytical and experimental research to develop a new seismic design methodology for precast concrete diaphragms. *Journal of Structural Engineering* 139: 1192–1204.

Ghosh SK and Cleland NM (2012) Performance of precast concrete building structures. *Earthquake Spectra* 28: 349–384.

Gonzalez A, Spacone E and Nascimbene R (2017) Performance-based seismic design framework for RC floor diaphragms in dual systems. *Procedia Engineering* 199: 3546–3551.

Henry RS, Dizhur D, Elwood KJ, Hare J and Brunsdon D (2017) Damage to concrete buildings with precast floors during the 2016 Kaikoura earthquake. *Bulletin of the New Zealand Society for Earthquake Engineering* 50: 174–186.

Iverson JK and Hawkins NM (1994) Performance of precast/prestressed building structures during Northridge earthquake. *PCI Journal* 39: 38–55.

Kam WY, Pampanin S and Elwood K (2011) Seismic performance of reinforced concrete buildings in the 22 February Christchurch (Lyttleton) earthquake. Bulletin of the New Zealand Society for Earthquake Engineering, 44(4), 239–278, December 2011. Available at: https://www.nzsee.org.nz/db/Bulletin/Archive/44%284%290239.pdf (accessed 29 September 2025).

Kuramoto H (2006) Seismic design codes for buildings in Japan. *Journal of Disaster Research* 1: 341–356.

López OA and Cruz M (1996) Number of modes for the seismic design of buildings. *Earthquake Engineering & Structural Dynamics* 25: 837–855.

Mayorga CF and Tsampras G (2022) Validation of seismic design provisions for diaphragms and assessment of higher-mode responses on earthquake-resistant buildings. In: Proceedings of the 2022 Strong-Motion Instrumentation Program (SMIP) Seminar on Utilization of Strong-Motion Data, Sacramento, CA, September 15, 2022. California Geological Survey, Sacramento, CA. Available at: https://www.conservation.ca.gov/cgs/pages/program-smi/seminar/smip22_toc.aspx (accessed 29 September 2025).

Mayorga CF and Tsampras G (2025) Validation of seismic design provisions for diaphragms and assessment of higher-mode responses on earthquake-resistant buildings. Available at: https://doi.org/10.17603/ds2-jnf5-e909.

Miranda E and Taghavi S (2005) Approximate floor acceleration demands in multistory buildings. I: Formulation. *Journal of Structural Engineering* 131: 203–211.

Moehle JP, Hooper JD and Meyer TR (2016) *Seismic design of cast-in-place concrete diaphragms, chords, and collectors: A guide for practicing engineers second edition*. Tech. Rep. NIST GCR 16-917-42. Gaithersburg, MD: National Institute of Standards and Technology.

NZS1170.5 (2004) NZS 1170.5:2004 (Includes Amdt 1). Standards New Zealand. Available at: https://www.standards.govt.nz/shop/nzs-1170-52004-includes-amdt-1/ (accessed 29 September 2025).

Panagiotou M and Restrepo JI (2009) Dual-plastic hinge design concept for reducing higher-mode effects on high-rise cantilever wall buildings. *Earthquake Engineering & Structural Dynamics* 38: 1359–1380.

Panagiotou M and Restrepo JI (2011) Displacement-based method of analysis for regular reinforced-concrete wall buildings: Application to a full-scale 7-story building slice tested at UC–San Diego. *Journal of Structural Engineering* 137: 677–690.

Panagiotou M, Restrepo JI and Conte JP (2011) Shake-table test of a Full-Scale 7-story building slice. Phase I: Rectangular wall. *Journal of Structural Engineering* 137: 691–704.

Priestley MJ and Amaris AD (2002) *Dynamic Amplification of Seismic Moments and Shear Forces in Cantilever Walls*. Pavia: IUSS Press.

Priestley MJN (2000) Performance based seismic design. *Bulletin of the New Zealand Society for Earthquake Engineering* 33: 325–346.

Priestley MJN, Calvi GM and Kowalsky MJ (2007) *Displacement Based Seismic Design of Structures*. 1st ed. Pavia: IUSS Press.

Rodriguez ME, Restrepo JI and Carr AJ (2002) Earthquake-induced floor horizontal accelerations in buildings. *Earthquake Engineering & Structural Dynamics* 31: 693–718.

Saatcioglu M, Mitchell D, Tinawi R, Gardner NJ, Gillies AG, Ghobarah A, Anderson DL and Lau D (2001) The August 17, 1999, Kocaeli (Turkey) Earthquake—damage to structures. *Canadian Journal of Civil Engineering* 28: 715–737.

Şafak E and Çelebi M (1990) Method to estimate center of rigidity using vibration recordings. *Journal of Structural Engineering* 116: 85–97.

Scarry JM (2014) Floor diaphragms – Seismic bulwark or Achilles'heel. In: Proceedings of the 2014 NZSEE Conference, Auckland, New Zealand, 21–23 March 2014. Available at: https://www.nzsee.org.nz/db/2014/oral/19_Scarry.pdf (accessed 29 September 2025).

Sewell RT, Cornell CA, Toro GR and McGuire RK (1986) *A study of factors influencing floor response spectra in nonlinear multi-degree-of-freedom structures*. Tech. Rep. Stanford, CA: Stanford University.

Soules JG, Bachman RE and Silva JF (2016) Chilean Standard NCh433.Of96: Seismic Design of Buildings (English translation). In: Chile Earthquake of 2010: Assessment of Industrial Facilities around Concepción. Reston, VA: American Society of Civil Engineers. Available at: https://doi.org/10.1061/9780784413647.ap01 (accessed September 29, 2025).

Tsampras G, Sause R, Zhang D, Fleischman RB, Restrepo JI, Mar D and Maffei J (2016) Development of deformable connection for earthquake-resistant buildings to reduce floor accelerations and force responses. *Earthquake Engineering & Structural Dynamics* 45: 1473–1494.

Van Rossum G and Drake FL (2009) *Python 3 Reference Manual*. Scotts Valley, CA: CreateSpace.

Wallace JW, Massone LM, Bonelli P, Dragovich J, Lagos R, Lüders C and Moehle J (2012) Damage and implications for seismic design of RC structural wall buildings. *Earthquake Spectra* 28: 281–299.

Wiebe L and Christopoulos C (2009) Mitigation of higher mode effects in base-rocking systems by using multiple rocking sections. *Journal of Earthquake Engineering* 13: 83–108.

Xiang Y, Naeim F and Zareian F (2020) Evaluation of natural periods and modal damping ratios for seismic design of building structures. *Earthquake Spectra* 36: 629–646.

Appendix 1

Symbols

This appendix provides a comprehensive list of all the symbols and their definitions as used throughout the research article.

$C_{px}^{(1)}$: Design acceleration coefficient at level x per ASCE/SEI 7-22 Section 12.10.1, [g]. $(F_{px}^{(1)}/w_{px})$

$C_{px,m}^{(1)}$: Design-based intensity-dependent acceleration coefficient at level x based on ASCE/SEI 7-22 Section 12.10.1 computed using the modification approach m, [g].

$C_{p0}^{(3)}$: Design acceleration coefficient at the base per ASCE/SEI 7-22 Section 12.10.3, [g].

$C_{pi}^{(3)}$: Design acceleration coefficient at 80% of h_n per ASCE/SEI 7-22 Section 12.10.3, [g].

$C_{pn}^{(3)}$: Design acceleration coefficient at h_n per ASCE/SEI 7-22 Section 12.10.3, [g].

$C_{px}^{(3)}$: Design acceleration coefficient at level x per ASCE/SEI 7-22 Section 12.10.3, [g].

$C_{px,m}^{(3)}$: Design-based intensity-dependent acceleration coefficient at level x based on ASCE/SEI 7-22 Section 12.10.3 computed using modification approach m, [g].

C_s: seismic response coefficient determined in ASCE/SEI 7-22 Section 12.8.1.1, [g].

C_{s2}: Higher-mode seismic response coefficient, [g].

C_{vi}: Vertical distribution factor at level i.

C_d: Deflection amplification factor.

$e_{\text{factor},x,m}^{(1)}$: Relative error of the design-based intensity-dependent acceleration coefficient factor based on ASCE/SEI 7-22 Section 12.10.1 computed using the modification approach m relative to the peak floor acceleration factor at the center of rigidity at level x. $((C_{px,m}^{(1)}/C_{p0,m}^{(1)} - PFA_x/PGA)/(PFA_x/PGA))$

$e_{\text{mag},x,m}^{(1)}$: Relative error of the design-based intensity-dependent acceleration coefficient based on ASCE/SEI 7-22 Section 12.10.1 computed using the modification approach m relative to the peak floor acceleration at the center of rigidity at level x. $((C_{px,m}^{(1)} - PFA_x)/PFA_x)$

$e_{\text{factor},x,m}^{(3)}$: Relative error of the design-based intensity-dependent acceleration coefficient factor based on ASCE/SEI 7-22 Section 12.10.3 computed using the modification approach m relative to the peak floor acceleration factor at the center of rigidity at level x. $((C_{px,m}^{(3)}/C_{p0,m}^{(3)} - PFA_x/PGA)/(PFA_x/PGA))$

$e^{(3)}_{\text{mag},x,m}$: Relative error of the design-based intensity-dependent acceleration coefficient based on ASCE/SEI 7-22 Section 12.10.3 computed using the modification approach m relative to the peak floor acceleration at the center of rigidity at level x. $((C^{(3)}_{px,m} - PFA_x)/PFA_x)$

$\bar{e}^{(1)}_{\text{factor},m}$: Average of the absolute value of the error $e^{(1)}_{\text{factor},x,m}$ over the height of the building station.

$\bar{e}^{(1)}_{\text{mag},m}$: Average of the absolute value of the error $e^{(1)}_{\text{mag},x,m}$ over the height of the building station.

$\bar{e}^{(3)}_{\text{factor},m}$: Average of the absolute value of the error $e^{(3)}_{\text{factor},x,m}$ over the height of the building station.

$\bar{e}^{(3)}_{\text{mag},m}$: Average of the absolute value of the error $e^{(3)}_{\text{mag},x,m}$ over the height of the building station.

$F^{(1)}_{px}$: Floor diaphragm design force at level x per ASCE/SEI 7-22 Section 12.10.1, [kN].

$F^{(3)}_{px}$: Floor diaphragm design force at level x per ASCE/SEI 7-22 Section 12.10.3, [kN].

F_i: SFRS design force applied to level i, [kN].

h_i: Height from the base to level i, [m].

h_n: Height from the base to the level n, [m].

h_{sx}: Story height below level x, as defined in ASCE/SEI 7-22 Table 12.12-1, [m].

h_x: Height from the base to level x, [m].

I_e: Building importance factor.

k: Exponent used to compute the vertical distribution of the SFRS design forces.

m: Index denoting the modification approach applied to $C^{(j)}_{px}$ to obtain $C^{(j)}_{px,m}$, with $m = 1, \ldots, 6$.

N: Number of stories above the base.

n: The highest level of the SFRS of the building.

PFA_x: Peak floor acceleration at the center of rigidity at level x, [g].

PGA: Measured peak ground acceleration, [g].

R: Design force reduction factor.

R_m: Force reduction factor used in modification approach m. (See Table 1)

R_s: Floor diaphragm design force reduction factor.

$R_{\delta_{msd}}$: Force reduction factor estimate at the intensity level of the measured ground motion.

$R_{S_a}(T, h_x/h_n)$: Spectral response factor at the normalized height h_x/h_n. $(S_a(T, h_x/h_n)/S_a(T, h_x/h_n = 0.0))$

$r_{S_a,m}$: Scaling factor used in modification approach m to account for the intensity of the measured ground motion. (See Table 1)

$r^1_{S_a}$: Ratio between the 5% damped ground spectral response acceleration at T_1 and design spectral response acceleration at T_1. $(S_a(T_1)/S_{ad}(T_1))$

$r^{12}_{S_a}$: Ratio between the square root of the sum of the squares of the 5% damped ground spectral response acceleration at the first two modal periods and squared root of the squares of the design spectral response acceleration at the first two modal periods. $\left(\sqrt{S_a(T_1)^2 + S_a(T_2)^2}/\sqrt{S_{ad}(T_1)^2 + S_{ad}(T_1)^2}\right)$

$r^{123}_{S_a}$: Ratio between the square root of the sum of the squares of the 5% damped ground spectral response acceleration at the first three modal periods and squared root of the squares of the design spectral response acceleration at the first three modal periods. $\left(\sqrt{S_a(T_1)^2 + S_a(T_2)^2 + \overline{S_a(T_3)^2}}/\sqrt{S_{ad}(T_1)^2 + S_{ad}(T_2)^2 + S_{ad}(T_3)^2}\right)$

$r^{(1)}_{\text{factor},x,m}$: Ratio between the peak floor acceleration factor at the center of rigidity and design-based intensity-dependent acceleration coefficient factor at level x based on ASCE/SEI 7-22 Section 12.10.1 computed using the modification approach m. $((PFA_x/PGA)/(C^{(1)}_{px,m}/C^{(1)}_{p0,m}))$

$r^{(1)}_{\text{mag},x,m}$: Ratio between the peak floor acceleration at the center of rigidity and design-based intensity-dependent acceleration coefficient at level x based on ASCE/SEI 7-22 Section 12.10.1 computed using the modification approach m. $(PFA_x/C^{(1)}_{px,m})$

$r^{(3)}_{\text{factor},x,m}$: Ratio between the peak floor acceleration factor at the center of rigidity and design-based intensity-dependent acceleration coefficient factor at level x based on ASCE/SEI 7-22 Section 12.10.3 computed using the modification approach m. $((PFA_x/PGA)/(C^{(3)}_{px,m}/C^{(3)}_{p0,m}))$

$r^{(3)}_{\text{mag},x,m}$: Ratio between the peak floor acceleration at the center of rigidity and design-based intensity-dependent acceleration coefficient at level x based on ASCE/SEI 7-22 Section 12.10.3 computed using the modification approach m. $(PFA_x/C^{(3)}_{px,m})$

$\bar{r}^{(1)}_{\text{factor},m}$: Average of the ratio $r^{(1)}_{\text{factor},x,m}$ over the height of the building station.

$\bar{r}^{(1)}_{\text{mag},m}$: Average of the ratio $r^{(1)}_{\text{mag},x,m}$ over the height of the building station.

$\mathrm{r}^{(3)}_{\text{factor},m}$: Average of the ratio $r^{(3)}_{\text{factor},x,m}$ over the height of the building station.

$\bar{r}^{(3)}_{\text{mag},m}$: Average of the ratio $r^{(3)}_{\text{mag},x,m}$ over the height of the building station.

S_{D1}: Design, 5% damped, spectral response acceleration parameter at a period of 1 s, [g].

S_{DS}: Design, 5% damped, spectral response acceleration parameter at short periods, [g].

$S_{ad}(T)$: Design spectral response acceleration, [g].

$S_a(T, h_x/h_n)$: 5% damped spectral response acceleration at the normalized height h_x/h_n, [g].

$S_a(T)$: 5% damped spectral response acceleration at the ground level, [g]. $(S_a(T, h_x/h_n = 0.0))$

T_i: i^{th} translational mode period, [s].

V: SFRS base shear required for design, [kN].

V_E: Force that would be developed in the SFRS if the system remained entirely linear-elastic for the design-level earthquake ground motion, [kN].

V_{max}: Actual maximum strength of the system reaching the inelastic-plastic deformation, [kN].

w_i: Weight tributary to level i, [kN].

w_{px}: Weight tributary to the floor diaphragm at level x, [kN].

$\left(x^*_g, y^*_g\right)$: Location coordinates of the center of rigidity at each sufficiently instrumented floor of a building station, [m].

z_s: Mode shape factor.

Γ_{m1}: First-mode contribution factor.

Γ_{m2}: Higher-mode contribution factor.

Δ_a: Design upper limit or allowable story drift given in ASCE/SEI 7-22 Table 12.12-1 for $h_{sx} = h_n$, [m].

δ: Roof drift of the SFRS corresponding to the design-level earthquake ground motion assuming that the system has reached the inelastic-plastic response, [m].

δ_E: Roof drift of the SFRS corresponding to V_E, [m].

δ_{msd}: Roof drift induced by the measured ground motion, [m].

Ω_0: Design overstrength factor.

$\Omega_{0,m}$: Overstrength factor used in modification approach m. (See Table 1)

$\Omega_{0\delta_{msd}}$: Overstrength factor estimate at the intensity level of the measured ground motion.

Appendix 2

Summary of workflow for data processing

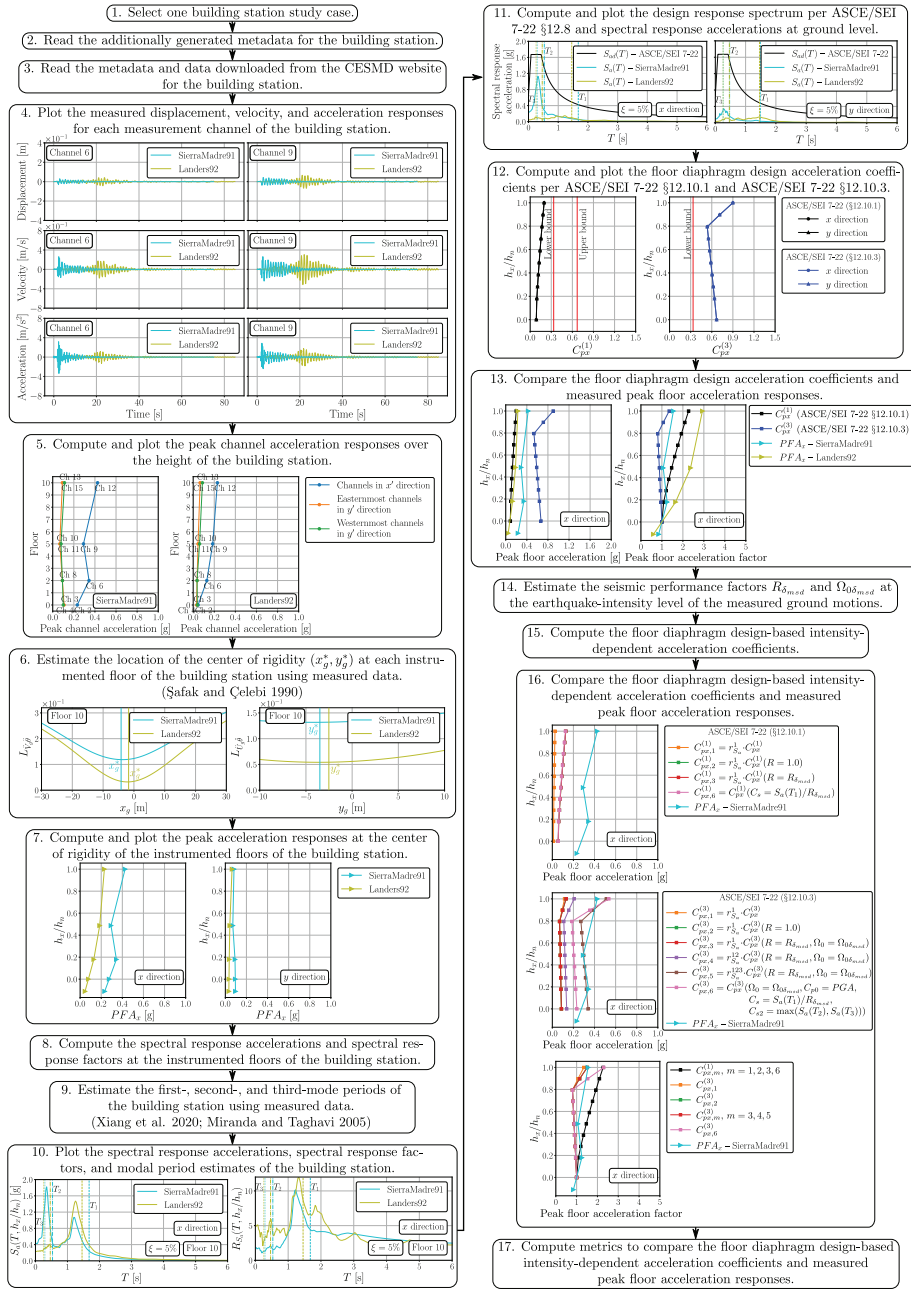


Figure 14. Detailed workflow for processing and analyzing CSMIP strong-motion data and metadata.